energies

MDPI

Article

Analytical Model for Rate-Transient Analysis of Shale Oil Wells Considering Multiphase Flow, Threshold Pressure Gradient, and Stress Sensitivity

Zhen Li [1], Kai Xu [1], Ping Guo [2], Xiaoli Yang [3], Yuyi Shen [1] and Junjie Ren [3,*]

[1] Research Institute of Exploration and Development, PetroChina Changqing Oilfield Company, Xi'an 710018, China; lizhenlz_cq@petrochina.com.cn (Z.L.); xukai01_cq@petrochina.com.cn (K.X.); shyuy_cq@petrochina.com.cn (Y.S.)
[2] State Key Laboratory of Oil and Gas Reservoir Geology and Exploitation, Southwest Petroleum University, Chengdu 610500, China; guopingswpi@vip.sina.com
[3] School of Sciences, Southwest Petroleum University, Chengdu 610500, China; 15730239083@163.com
* Correspondence: renjunjie1900@126.com; Tel.: +86-028-83037669

Abstract

Shale oil reservoirs exhibit ultralow permeability and complex pore structures, which result in non-Darcy low-velocity flow and cause permeability to be stress-sensitive. Moreover, two-phase flow of oil and gas frequently occurs during the depletion of shale oil reservoirs. Consequently, investigating the rate-transient behavior of shale oil wells necessitates comprehensive consideration of multiphase flow, threshold pressure gradients, and stress sensitivity. Although numerous analytical models exist for rate-transient analysis of multistage fractured horizontal wells, none of them simultaneously incorporate these critical factors. In this study, we extend the classical five-region model to incorporate multiphase flow, threshold pressure gradients, and stress sensitivity. The proposed model is solved using Pedrosa's transformation, perturbation theory, the Laplace transform, and the Stehfest numerical inversion method. A systematic analysis of the influence of various parameters on the oil production rate and cumulative oil production is conducted, and a field case study is presented to validate the applicability and effectiveness of the model. It is found that the permeability modulus of the main fracture, the half-length of the main fracture, and the threshold pressure gradient of the unstimulated reservoir have a significant influence on cumulative oil production spanning 20 years. With a 100% relative input error, these parameters result in prediction errors of 23.77%, 16.65%, and 17.78%, respectively. In contrast, the threshold pressure gradient of the main fracture and the threshold pressure gradient of the stimulated reservoir have a negligible impact; under the same level of input error (100%), they cause only 0.36% and 0.48% prediction errors in the 20-year cumulative oil production period, respectively. This research provides an efficient and reliable framework for analyzing production data and forecasting shale oil well performance.

Keywords: analytical modeling; rate transient analysis; multistage fractured horizontal well; shale oil reservoirs; multiphase flow; non-Darcy effect

Check for updates

Academic Editor: Krzysztof Skrzypkowski

Received: 28 November 2025
Revised: 30 December 2025
Accepted: 6 January 2026
Published: 9 January 2026

Copyright: © 2026 by the authors. Licensee MDPI, Basel, Switzerland. This article is an open access article distributed under the terms and conditions of the Creative Commons Attribution (CC BY) license.

1. Introduction

Shale oil reservoirs differ from conventional reservoirs by exhibiting ultralow permeability and highly complex pore structures, which result in significant non-Darcy effects, such as threshold pressure gradients and stress sensitivity, during production [1–6]. Shale

oil reservoirs are recognized as a type of reservoir that exhibits non-negligible two-phase (oil and gas) flow during depletion [7,8]. The study of fluid flow through porous media has garnered significant attention from the scientific community [9–11]. Although the implementation of horizontal wells combined with multistage volume fracturing technology has enabled the effective development of shale reservoirs and significantly enhanced the production capacity of shale oil wells [12–17], the complex well architecture and fracture networks substantially affect multiphase transport, thereby increasing the complexity of rate-transient analysis. The development of novel methodologies for rate-transient analysis, which integrate the influence of non-Darcy effects and multiphase flow, is crucial for accurately predicting the production evolution of shale oil wells, estimating single-well estimated ultimate recovery (EUR), optimizing fracturing designs, and formulating efficient production systems.

Currently, the approaches commonly employed for rate-transient analysis of shale oil wells can be comprehensively classified into three categories: empirical formula methods [18–22], analytical modeling methods [23–26], and numerical simulation methods [27–31]. Empirical formula methods, typified by models such as Arps [32], SEPD [33], and Duong [34], are characterized by their operational simplicity and relatively low data requirements. However, these methods fail to accurately represent the underlying flow physics and are typically more suitable for wells with long production histories that have entered the boundary-dominated flow regime. Numerical simulation methods involve the development of elaborate numerical models to represent complex geological structures, fracture networks, and boundary conditions. Nevertheless, constructing such models and performing history matching require numerous input parameters, substantial computational resources, and long runtimes and often introduce greater uncertainty due to parameter complexity. In contrast, analytical modeling methods derive solutions from the governing flow equations using appropriate linearization or transformation techniques. These methods are computationally efficient, allow for parameter sensitivity analysis and dimensionless generalization, and explicitly reveal the mechanistic influences of physical processes—such as flow regimes, stress sensitivity, and threshold pressure gradients—on productivity. In recent years, researchers both domestically and internationally have proposed various analytical and semi-analytical models to characterize flow behavior in various reservoirs developed using volume-fractured horizontal wells. Among these, linear flow models are the most extensively utilized. As fundamental tools for clarifying complex flow mechanisms, analytical models can be further subdivided into single-phase and multiphase models.

Single-phase analytical models, such as the tri-linear and five-linear flow models, are firmly based on rigorous principles of flow mechanics governing porous media. These models can systematically characterize the entire evolution of the bottomhole pressure response, ranging from early transient (non-stabilized) flow to late boundary-dominated flow. Owing to their robust underlying flow physics and high computational efficiency, these models have been widely employed in early research. For example, Deng et al. [35], Zhang et al. [36], and Haeri et al. [37] subsequently expanded the five-linear model by incorporating non-linear flow mechanisms in both heterogeneous and homogeneous multi-fractured systems. Ji et al. [38], within a five-region linear-flow framework, incorporated threshold pressure gradients and stress sensitivity effects and clarified their influences on the well performance for multi-fractured horizontal wells in tight formations. Shi and Lu [39] put forward a novel fractal-composite flow model based on the five-linear model. They introduced the distribution of secondary fracture spacing and width using fractal theory and verified the model's applicability in production history matching and recoverable reserve estimation. Furthermore, Yuan et al. [40] and Zeng et al. [41,42]

extended the five-linear model to a seven-linear model. In addition, Guo et al. [43] put forward a seven-region semi-analytical mathematical model for a fractal oil reservoir, aiming to explore the influence mechanism of heterogeneous fracture parameters on the productivity of multi-fractured horizontal wells. Currently, single-phase analytical models have matured significantly and are widely employed in productivity prediction and dynamic analysis of shale oil and gas. However, these models are primarily applicable to the single-phase flow stage when the reservoir pressure remains above the saturation pressure. Once the pressure drops below the bubble point, their ability to capture phase-behavior changes becomes limited, thereby restricting their applicability under multiphase production conditions.

Multiphase analytical models, based on multiphase flow theory, have been developed to provide approximate analytical solutions that describe the flow behavior of two-phase and even three-phase systems. Although these models emerged relatively recently, they have increasingly become a central focus in research due to their closer alignment with the multiphase flow characteristics commonly observed in shale hydrocarbon production. Shojaei and Tajer [44] integrated a tri-linear flow pressure field with the mass conservation equation, incorporating relative permeability to differentiate the production of oil and water phases. Their approach enabled the prediction of production characteristics for both phases during depletion production. Zhang et al. [45] put forward an analytical method for early production data that accounts for multiphase flow by quantifying the relationship between fluid saturation and pressure. Similarly, Behmanesh et al. [46] presented a semi-analytical model for wells operating under boundary-dominated flow conditions, thereby establishing a theoretical basis for analyzing multiphase production data. Furthermore, Wu et al. [47] developed an approximate semi-analytical method for two-phase flow production analysis. This method employs a linear flow model that incorporates multi-segment fracture regions and stimulated reservoirs. It simplifies the primary governing equation using the production gas-oil ratio (GOR) and provides a solution in the Laplace domain, thereby facilitating history matching and long-term prediction for multi-stage fractured horizontal wells. Luo et al. [48] put forward a rate-transient analysis approach to interpret production data in tight volatile oil reservoirs. Their method focused on an analysis of the comprehensive flow regime and established an empirical relationship between fluid saturation and pressure in such reservoirs. Ke et al. [49] integrated two-phase flow in the reservoir with the flow in the wellbore, thereby developing a model for calculating oil–gas two-phase production in horizontal wells. They allocated production based on the relative permeability of oil and gas and validated the model's feasibility by comparing it with field data. Bai et al. [50] developed a prediction method that characterizes the relationship between full-path oil saturation and pressure in tight condensate gas wells, subsequently formulating a transient production prediction model that accounts for multiphase flow. Zhang et al. [51] developed a three-phase productivity equation to evaluate the production performance of multiphase flow in horizontal wells in water-bearing condensate gas reservoirs. Furthermore, Wei et al. [52], based on the five-linear flow theory, integrated the liquid-absorption mechanism with material balance principles to establish a multiphase production prediction model applicable to volume-fractured horizontal wells undergoing cyclic water injection.

In summary, although previous studies have made progress in developing multiphase analytical models, these models generally have limited scopes, which hinder their ability to comprehensively capture the actual production conditions of shale oil wells. To the best of our knowledge, no existing analytical model simultaneously accounts for the threshold pressure gradient, stress sensitivity, and multiphase flow effects when predicting the production performance of hydraulically fractured horizontal wells in shale oil reservoirs.

Therefore, building on the five-region model [25], this study proposes a novel analytical framework that, for the first time, integrates all three factors—threshold pressure gradient, stress sensitivity, and multiphase flow—to accurately predict well productivity under realistic reservoir conditions.

2. Physical Models

After volume fracturing of a horizontal well in a shale oil reservoir, a complex fracture network is generated, and the flow regions are partitioned as illustrated in Figure 1. Region 1, Region 2, and Region 3 represent unstimulated portions of the reservoir that remain unaffected by the fracturing process, thereby exhibiting extremely low permeability. In contrast, Region 4 corresponds to the stimulated reservoir. Owing to hydraulic fracturing, this region develops a complex fracture network with relatively high permeability. Region 5 represents the main fracture, which is characterized by fracture conductivity. Fluid flows from the unstimulated reservoir (Region 1, Region 2, and Region 3) into the stimulated reservoir (Region 4), then into the main fracture (Region 5), and finally reaches the horizontal wellbore. The other fundamental assumptions for the model are as follows:

(1) The reservoir has uniform thickness, and the fractures fully penetrate it.
(2) The reservoir exhibits heterogeneity, with distinct reservoir parameters between the unstimulated and stimulated regions.
(3) The reservoir temperature remains constant, and oil and gas are considered to be compressible fluids.
(4) The effects of the threshold pressure gradient and stress sensitivity are considered.
(5) Considering phase changes in oil and gas, the high-pressure physical properties of the fluids vary with pressure.

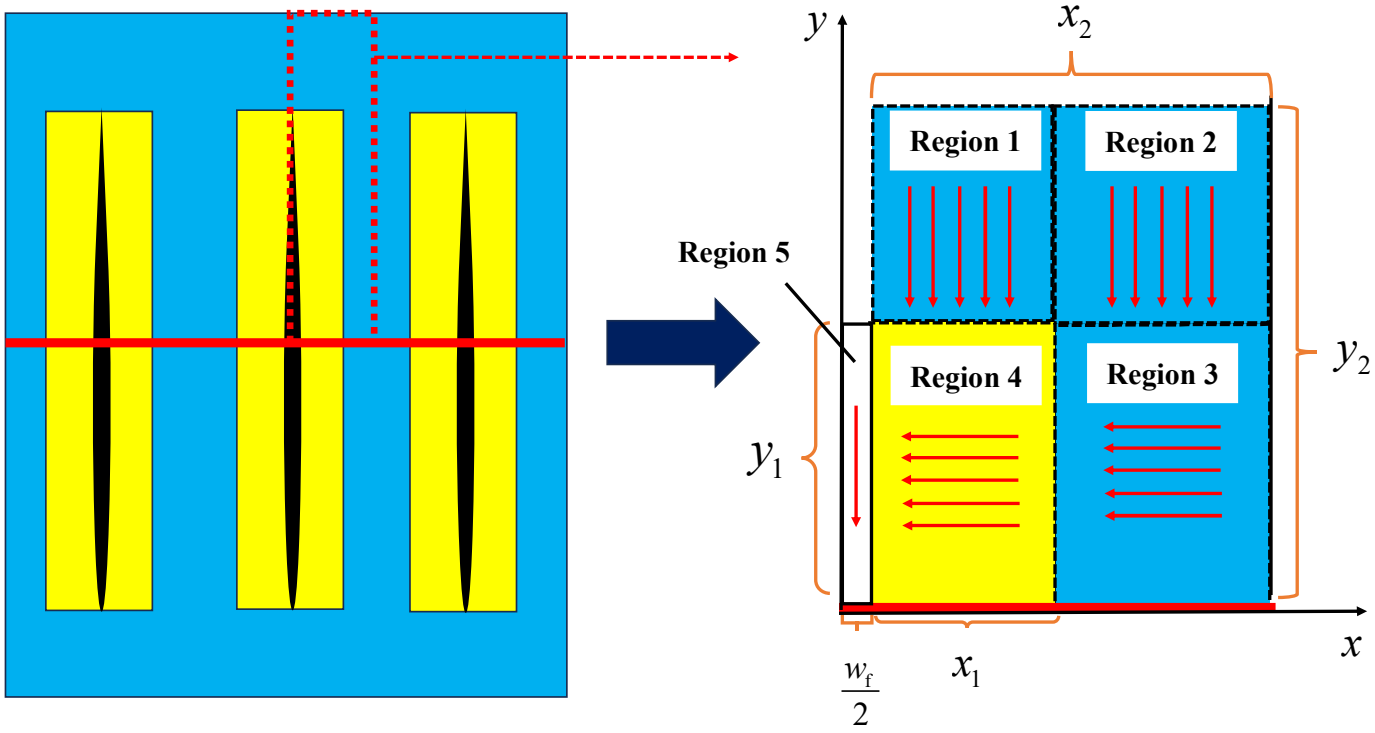


Figure 1. Schematic of the physical model for a volume-fractured horizontal well.

3. Mathematical Models

Based on the physical model, the five-linear model [25] is developed by incorporating multiphase flow, threshold pressure gradient, and stress sensitivity effects. The detailed procedures for deriving and solving the mathematical model of shale oil wells, which take into account multiphase flow, threshold pressure gradients, and stress sensitivity, are presented as follows.

3.1. Model Establishing

3.1.1. Region 1

To account for the multiphase flow [48,50], threshold pressure gradient, and stress sensitivity [26], the governing partial differential equation for the primary phase in Region 1 is employed, with

$$\frac{\partial}{\partial y}\left[\frac{K_1(p_1)K_{\mathrm{ro}}}{\mu_{\mathrm{o}}B_{\mathrm{o}}}\left(\frac{\partial p_1}{\partial y}-\lambda_1\right)+R_{\mathrm{v}}\frac{K_1(p_1)K_{\mathrm{rg}}}{\mu_{\mathrm{g}}B_{\mathrm{g}}}\left(\frac{\partial p_1}{\partial y}-\lambda_1\right)\right]=\frac{\phi_1}{C}\frac{\partial}{\partial t}\left(\frac{S_{\mathrm{o}}}{B_{\mathrm{o}}}+R_{\mathrm{v}}\frac{S_{\mathrm{g}}}{B_{\mathrm{g}}}\right), \quad (1)$$

where the subscript 1 denotes Region 1; p is the pressure (MPa); $K(p)$ is the pressure-dependent permeability (mD); K_{ro} is the oil's relative permeability (fraction); K_{rg} is the gas's relative permeability (fraction); μ_{o} is the oil's viscosity (mPa · s); μ_{g} is the gas's viscosity (mPa · s); B_{o} is the oil volume factor ($\mathrm{m}^3/\mathrm{m}^3$); B_{g} is the gas volume factor ($\mathrm{m}^3/\mathrm{m}^3$); λ is the threshold pressure gradient (MPa/m); y is the y-coordinate (m); t is time (d); ϕ represents porosity (fraction); R_{v} is the solution's oil–gas ratio ($\mathrm{m}^3/\mathrm{m}^3$); S_{o} represents oil saturation (fraction); S_{g} represents gas saturation (fraction); and C is the unit conversion coefficient, which is taken as 0.0864 here.

In order to linearize the governing equation for the primary phase, the two-phase pseudopressure is defined as [48,50]

$$p_{\mathrm{po}j}=\int_{p_{\mathrm{ref}}}^{p_j}\left(\frac{K_{\mathrm{ro}}}{\mu_{\mathrm{o}}B_{\mathrm{o}}}+R_{\mathrm{v}}\frac{K_{\mathrm{rg}}}{\mu_{\mathrm{g}}B_{\mathrm{g}}}\right)\mathrm{d}p_j, \quad (2)$$

where the subscript j represents Region j, where j takes the values 1, 2, 3, 4, and 5; p_{ref} is the reference pressure (MPa); and p_{po} is the two-phase pseudopressure (MPa/(mPa · s)).

The pressure-dependent permeability of Region j is described as [53]

$$K_j(p_j)=K_{\mathrm{i}j}\exp\left[-\gamma_{\mathrm{o}j}\left(p_{\mathrm{poi}}-p_{\mathrm{po}j}\right)\right], \quad (3)$$

where $K_{\mathrm{i}j}$ is the initial permeability of Region j (mD); $\gamma_{\mathrm{o}j}$ is the pseudo-permeability modulus of Region j ((mPa · s)/MPa); and p_{poi} is the initial pseudopressure (MPa/(mPa · s)).

Substituting Equations (2) and (3) into Equation (1) yields

$$K_{\mathrm{i}1}e^{-\gamma_{\mathrm{o}1}\left(p_{\mathrm{poi}}-p_{\mathrm{po}1}\right)}\left[\frac{\partial^2 p_{\mathrm{po}1}}{\partial y^2}+\gamma_{\mathrm{o}1}\left(\frac{\partial p_{\mathrm{po}1}}{\partial y}\right)^2-G_{\mathrm{o}1}\frac{\partial p_{\mathrm{po}1}}{\partial y}\right]=\frac{\phi_1\eta_{\mathrm{o}1}}{C}\frac{\partial p_{\mathrm{po}1}}{\partial t}, \quad (4)$$

where $G_{\mathrm{o}j}$ is the generalized threshold pressure coefficient of Region $j(j=1,2,3,4,5)$, while $\eta_{\mathrm{o}j}$ is the generalized compressibility/mobility ratio of Region $j(j=1,2,3,4,5)$, which are both, respectively, expressed as

$$G_{\mathrm{o}j}=\gamma_{\mathrm{o}j}\lambda_j\left(\frac{K_{\mathrm{ro}}}{\mu_{\mathrm{o}}B_{\mathrm{o}}}+R_{\mathrm{v}}\frac{K_{\mathrm{rg}}}{\mu_{\mathrm{g}}B_{\mathrm{g}}}\right)+\frac{\lambda_j\frac{\partial}{\partial p_j}\left(\frac{K_{\mathrm{ro}}}{\mu_{\mathrm{o}}B_{\mathrm{o}}}+R_{\mathrm{v}}\frac{K_{\mathrm{rg}}}{\mu_{\mathrm{g}}B_{\mathrm{g}}}\right)}{\frac{K_{\mathrm{ro}}}{\mu_{\mathrm{o}}B_{\mathrm{o}}}+R_{\mathrm{v}}\frac{K_{\mathrm{rg}}}{\mu_{\mathrm{g}}B_{\mathrm{g}}}}, \quad (5)$$

$$\eta_{oj} = \frac{\frac{\partial}{\partial p_j}\left(\frac{S_o}{B_o} + R_v \frac{S_g}{B_g}\right)}{\frac{K_{ro}}{\mu_o B_o} + R_v \frac{K_{rg}}{\mu_g B_g}}. \tag{6}$$

Strictly speaking, G_{oj} and η_{oj} are functions of pressure. To derive an analytical solution and in accordance with previous studies [48,50], these parameters are assumed to be constant, with their values taken as averages.

The initial condition in Region 1 is

$$p_{po1}\big|_{t=0} = p_{poi}. \tag{7}$$

The outer boundary condition in Region 1 is given as

$$\left.\frac{\partial p_{po1}}{\partial y}\right|_{y=y_2} = 0, \tag{8}$$

where y_2 is the half-width of the reservoir (m).

The inner boundary condition in Region 1 is given by

$$p_{po1}\big|_{y=y_1} = p_{po4}\big|_{y=y_1}, \tag{9}$$

where y_1 is the half-length of the main fracture (m).

3.1.2. Region 2

The governing equation in Region 2 is given as

$$K_{i2} e^{-\gamma_{o2}(p_{poi}-p_{po2})}\left[\frac{\partial^2 p_{po2}}{\partial y^2} + \gamma_{o2}\left(\frac{\partial p_{po2}}{\partial y}\right)^2 - G_{o2}\frac{\partial p_{po2}}{\partial y}\right] = \frac{\phi_2 \eta_{o2}}{C}\frac{\partial p_{po2}}{\partial t}, \tag{10}$$

The initial condition in Region 2 is

$$p_{po2}\big|_{t=0} = p_{poi}. \tag{11}$$

The outer boundary condition in Region 2 is given as

$$\left.\frac{\partial p_{po2}}{\partial y}\right|_{y=y_2} = 0. \tag{12}$$

The inner boundary condition in Region 2 is given by

$$p_{po2}\big|_{y=y_1} = p_{po3}\big|_{y=y_1}. \tag{13}$$

3.1.3. Region 3

The governing equation in Region 3 is given as

$$\begin{aligned} &K_{i3} e^{-\gamma_{o3}(p_{poi}-p_{po3})}\left[\frac{\partial^2 p_{po3}}{\partial x^2} + \gamma_{o3}\left(\frac{\partial p_{po3}}{\partial x}\right)^2 - G_{o3}\frac{\partial p_{po3}}{\partial x}\right] \\ &+\frac{1}{y_1} K_{i2}\, e^{-\gamma_{o2}(p_{poi}-p_{po2})}\left[\frac{\partial p_{po2}}{\partial y} - \left(\frac{K_{ro}}{\mu_o B_o} + R_v \frac{K_{rg}}{\mu_g B_g}\right)\lambda_2\right]\Big|_{y=y_1} = \frac{\phi_3 \eta_{o3}}{C}\frac{\partial p_{po3}}{\partial t}. \end{aligned} \tag{14}$$

The initial condition in Region 3 is

$$p_{po3}\big|_{t=0} = p_{poi}. \tag{15}$$

The outer boundary condition in Region 3 is given as

$$\left.\frac{\partial p_{\mathrm{po3}}}{\partial x}\right|_{x=x_2} = 0, \tag{16}$$

where x_2 is the half-length between main fractures (m).

The inner boundary condition in Region 3 is given by

$$p_{\mathrm{po3}}\big|_{x=x_1} = p_{\mathrm{po4}}\big|_{x=x_1}, \tag{17}$$

where x_1 is the half-length of the stimulated reservoir for one main fracture (m).

3.1.4. Region 4

The governing equation in Region 4 is given as

$$\begin{aligned} &K_{\mathrm{i4}} e^{-\gamma_{\mathrm{o4}}(p_{\mathrm{poi}}-p_{\mathrm{po4}})}\left[\frac{\partial^2 p_{\mathrm{po4}}}{\partial x^2} + \gamma_{\mathrm{o4}}\left(\frac{\partial p_{\mathrm{po4}}}{\partial x}\right)^2 - G_{\mathrm{o4}}\frac{\partial p_{\mathrm{po4}}}{\partial x}\right] \\ &+\frac{1}{y_1}K_{\mathrm{i1}}\, e^{-\gamma_{\mathrm{o1}}(p_{\mathrm{poi}}-p_{\mathrm{po1}})}\left[\frac{\partial p_{\mathrm{po1}}}{\partial y} - \left(\frac{K_{\mathrm{ro}}}{\mu_{\mathrm{o}}B_{\mathrm{o}}} + R_{\mathrm{v}}\frac{K_{\mathrm{rg}}}{\mu_{\mathrm{g}}B_{\mathrm{g}}}\right)\lambda_1\right]\Big|_{y=y_1} = \frac{\phi_4\eta_{\mathrm{o4}}}{C}\frac{\partial p_{\mathrm{po4}}}{\partial t}. \end{aligned} \tag{18}$$

The initial condition in Region 4 is

$$p_{\mathrm{po4}}\big|_{t=0} = p_{\mathrm{poi}}. \tag{19}$$

The outer boundary condition in Region 4 is given as

$$K_{\mathrm{i3}}\, e^{-\gamma_{\mathrm{o3}}(p_{\mathrm{poi}}-p_{\mathrm{po3}})}\left[\frac{\partial p_{\mathrm{po3}}}{\partial x} - \left(\frac{K_{\mathrm{ro}}}{\mu_{\mathrm{o}}B_{\mathrm{o}}} + R_{\mathrm{v}}\frac{K_{\mathrm{rg}}}{\mu_{\mathrm{g}}B_{\mathrm{g}}}\right)\lambda_3\right]\Big|_{x=x_1} = K_{\mathrm{i4}}\, e^{-\gamma_{\mathrm{o4}}(p_{\mathrm{poi}}-p_{\mathrm{po4}})}\left[\frac{\partial p_{\mathrm{po4}}}{\partial x} - \left(\frac{K_{\mathrm{ro}}}{\mu_{\mathrm{o}}B_{\mathrm{o}}} + R_{\mathrm{v}}\frac{K_{\mathrm{rg}}}{\mu_{\mathrm{g}}B_{\mathrm{g}}}\right)\lambda_4\right]\Big|_{x=x_1}. \tag{20}$$

The inner boundary condition in Region 4 is given by

$$p_{\mathrm{po4}}\big|_{x=\frac{w_{\mathrm{f}}}{2}} = p_{\mathrm{po5}}\big|_{x=\frac{w_{\mathrm{f}}}{2}}. \tag{21}$$

3.1.5. Region 5

The governing equation in Region 5 is given as

$$\begin{aligned} &K_{\mathrm{i5}} e^{-\gamma_{\mathrm{o5}}(p_{\mathrm{poi}}-p_{\mathrm{po5}})}\left[\frac{\partial^2 p_{\mathrm{po5}}}{\partial y^2} + \gamma_{\mathrm{o5}}\left(\frac{\partial p_{\mathrm{po5}}}{\partial y}\right)^2 - G_{\mathrm{o5}}\frac{\partial p_{\mathrm{po5}}}{\partial y}\right] \\ &+\frac{2}{w_{\mathrm{f}}}K_{\mathrm{i4}}\, e^{-\gamma_{\mathrm{o4}}(p_{\mathrm{poi}}-p_{\mathrm{po4}})}\left[\frac{\partial p_{\mathrm{po4}}}{\partial x} - \left(\frac{K_{\mathrm{ro}}}{\mu_{\mathrm{o}}B_{\mathrm{o}}} + R_{\mathrm{v}}\frac{K_{\mathrm{rg}}}{\mu_{\mathrm{g}}B_{\mathrm{g}}}\right)\lambda_4\right]\Big|_{x=\frac{w_{\mathrm{f}}}{2}} = \frac{\phi_5\eta_{\mathrm{o5}}}{C}\frac{\partial p_{\mathrm{po5}}}{\partial t}. \end{aligned} \tag{22}$$

The initial condition in Region 5 is

$$p_{\mathrm{po5}}\big|_{t=0} = p_{\mathrm{poi}}. \tag{23}$$

The outer boundary condition in Region 5 is given as

$$\left.\frac{\partial p_{\mathrm{po5}}}{\partial y}\right|_{y=y_1} = 0. \tag{24}$$

The inner boundary condition in Region 5 is given by

$$p_{\mathrm{po5}}\big|_{y=0} = p_{\mathrm{powf}}, \tag{25}$$

where p_{powf} is the constant bottomhole pseudopressure (MPa/(mPa · s)).

Under constant bottomhole pressure conditions, the production rate of a shale oil well can be readily determined by

$$q_{\mathrm{o}} = 2Cn_{\mathrm{f}}w_{\mathrm{f}}hK_{\mathrm{i5}}\,e^{-\gamma_{\mathrm{o5}}(p_{\mathrm{poi}}-p_{\mathrm{po5}})}\left[\frac{\partial p_{\mathrm{po5}}}{\partial y}-\left(\frac{K_{\mathrm{ro}}}{\mu_{\mathrm{o}}B_{\mathrm{o}}}+R_{\mathrm{v}}\frac{K_{\mathrm{rg}}}{\mu_{\mathrm{g}}B_{\mathrm{g}}}\right)\lambda_5\right]\Bigg|_{y=0}, \tag{26}$$

where q_{o} is the oil production rate (m^3/d); n_{f} is the number of main fractures; and h is the thickness of reservoirs (m).

3.2. Model Solutions

3.2.1. Analytical Solution of Mathematical Models

Equations (1)–(26) constitute a non-linear mathematical model. To obtain an analytical solution, the pseudopressure drop and the Pedrosa transformation [53] are introduced as follows:

$$\Delta p_{\mathrm{po}j} = p_{\mathrm{poi}} - p_{\mathrm{po}j}, \tag{27}$$

$$\Delta p_{\mathrm{po}j} = -\frac{1}{\gamma_{\mathrm{o}j}}\ln\left(1-\gamma_{\mathrm{o}j}\tau_{\mathrm{o}j}\right), \tag{28}$$

where the subscript j represents Region j, where $j = 1, 2, 3, 4, 5$.

By substituting Equations (27) and (28) into Equation (4), the following results are obtained:

$$\frac{\partial^2\tau_{\mathrm{o1}}}{\partial y^2} - G_{\mathrm{o1}}\frac{\partial\tau_{\mathrm{o1}}}{\partial y} = \frac{\phi_1\eta_{\mathrm{o1}}}{CK_{\mathrm{i1}}}\frac{1}{1-\gamma_{\mathrm{o1}}\tau_{\mathrm{o1}}}\frac{\partial\tau_{\mathrm{o1}}}{\partial t}. \tag{29}$$

We introduced a perturbation to simplify the above weakened non-linear equation. The details of this perturbation for Region j are outlined below:

$$\tau_{\mathrm{o}j} = \tau_{\mathrm{o0}j} + \gamma_{\mathrm{o}j}\tau_{\mathrm{o1}j} + \gamma_{\mathrm{o}j}^2\tau_{\mathrm{o2}j} + \cdots, \tag{30}$$

$$\frac{1}{1-\gamma_{\mathrm{o}j}\tau_{\mathrm{o}j}} = 1 + \gamma_{\mathrm{o}j}\tau_{\mathrm{o}j} + \left(\gamma_{\mathrm{o}j}\tau_{\mathrm{o}j}\right)^2 + \cdots, \tag{31}$$

where $\tau_{\mathrm{o0}j}$, $\tau_{\mathrm{o1}j}$, and $\tau_{\mathrm{o2}j}$ are the zeroth-, first-, and second-order perturbation solutions of $\tau_{\mathrm{o}j}$ for Region j, respectively. It has been demonstrated that the zeroth-order perturbation provides a reliable approximation. The corresponding zeroth-order equation for Equation (29) is given below:

$$\frac{\partial^2\tau_{\mathrm{o01}}}{\partial y^2} - G_{\mathrm{o1}}\frac{\partial\tau_{\mathrm{o01}}}{\partial y} = \frac{\phi_1\eta_{\mathrm{o1}}}{CK_{\mathrm{i1}}}\frac{\partial\tau_{\mathrm{o01}}}{\partial t}. \tag{32}$$

The Laplace transform is defined as

$$\overline{\tau}(s) = \int_0^\infty \tau(t)e^{-st}\mathrm{d}t, \tag{33}$$

where τ is a variable related to time, s is the Laplace transform variable, and $\overline{\tau}$ is the variable in a Laplace space.

By applying the Pedrosa transformation and the Laplace transform to Equations (4)–(26), we obtain (see Appendix A for details)

$$\overline{q}_{\mathrm{o}} = -2Cn_{\mathrm{f}}w_{\mathrm{f}}hK_{\mathrm{i5}}\left[\left(\beta_5-\gamma_{\mathrm{o5}}\xi_{\mathrm{o5}}\right)\frac{\tau_{\mathrm{owf}}}{s}+\beta_5\frac{g_5(s)}{f_5(s)}+\frac{\xi_{\mathrm{o5}}}{s}\right], \tag{34}$$

where for detailed information on β_5, ξ_{o5}, τ_{owf}, $g_5(s)$, and $f_5(s)$, readers are referred to Appendix A.

Finally, the Stehfest algorithm [54] is utilized to transform $\bar{q}_o$ in the Laplace domain into q_o in the real domain, thereby obtaining oil production data that enables rate-transient analysis of shale oil wells.

3.2.2. Calculation of Two-Phase Pseudopressure and Non-Linear Parameters

Although the introduction of the two-phase pseudopressure (i.e., p_{poj}) and approximately constant non-linear parameters (e.g., G_{oj}, η_{oj}, and ξ_{oj}) has successfully linearized the mathematical model for an analytical solution, calculating the two-phase pseudopressure and determining the approximately constant values for the non-linear parameters remain challenging. Building on previous studies [48,50], the constant non-linear parameter values can be approximated by calculating the average of these parameters during the production process. Moreover, computing the two-phase pseudopressure is quite complex because it is necessary to correlate relative permeability with pressure. The key to this correlation lies in accurately determining the saturation–pressure relationship, which remains an open issue. In this study, the saturation–pressure relationship is derived from the constant volume depletion (CVD) path of PVT tests. Additionally, pressure-dependent PVT parameters, including the oil/gas volume factor, oil/gas viscosity, and the solution's oil–gas ratio, are also obtained from the PVT tests.

4. Results and Analyses

Based on the above mathematical model for volume-fractured horizontal wells in a shale oil reservoir, the oil production characteristics are investigated in detail. Furthermore, the influence of relevant parameters on oil production is discussed. Finally, a field case study is presented to demonstrate the application and effectiveness of the proposed analytical model.

4.1. Model Validation

It is evident that when the threshold pressure gradient and permeability modulus approach zero and multiphase flow effects are neglected, the proposed model reduces to a single-phase flow model. For verification, the simplified model is compared with the published Stalgorova–Mattar model [25]. The parameters used for model validation are listed in Table 1, and the comparative results are presented in Figure 2. As shown in Figure 2, the results from the simplified model exhibit strong agreement with those of the Stalgorova–Mattar model.

Table 1. Basic parameters used in the mathematical model for model validation.

Parameters	Value	Unit
Porosity of the unstimulated reservoir (Regions 1, 2, and 3)	0.1	fraction
Initial permeability of the unstimulated reservoir (Regions 1, 2, and 3)	0.01	mD
Threshold pressure gradient of the unstimulated reservoir (Regions 1, 2, and 3)	0	MPa/m
Permeability modulus of the unstimulated reservoir (Regions 1, 2, and 3)	0.0001	MPa^{-1}
Porosity of the stimulated reservoir (Region 4)	0.2	fraction
Initial permeability of the stimulated reservoir (Region 4)	1.0	mD
Threshold pressure gradient of the stimulated reservoir (Region 4)	0	MPa/m
Permeability modulus of the stimulated reservoir (Region 4)	0.0001	MPa^{-1}
Porosity of the main fracture (Region 5)	0.2	fraction
Conductivity of the main fracture (Region 5)	5.0	$mD \cdot m$
Threshold pressure gradient of the main fracture (Region 5)	0	MPa/m
Permeability modulus of the main fracture (Region 5)	0.0001	MPa^{-1}

Table 1. *Cont.*

Parameters	Value	Unit
Initial reservoir pressure	15.8	MPa
Oil viscosity	0.94	MPa·s
Bottomhole pressure	6.0	MPa
Oil volume factor	1.40	m^3/m^3
Reservoir thickness	14.5	m
Half-width of the reservoir	500	m
Number of main fractures	20	
Half-length of the main fracture	180	m
Width of the main fracture	0.02	m
Half-length of the stimulated reservoir for one main fracture	40	m
Half-length between main fractures	50	m

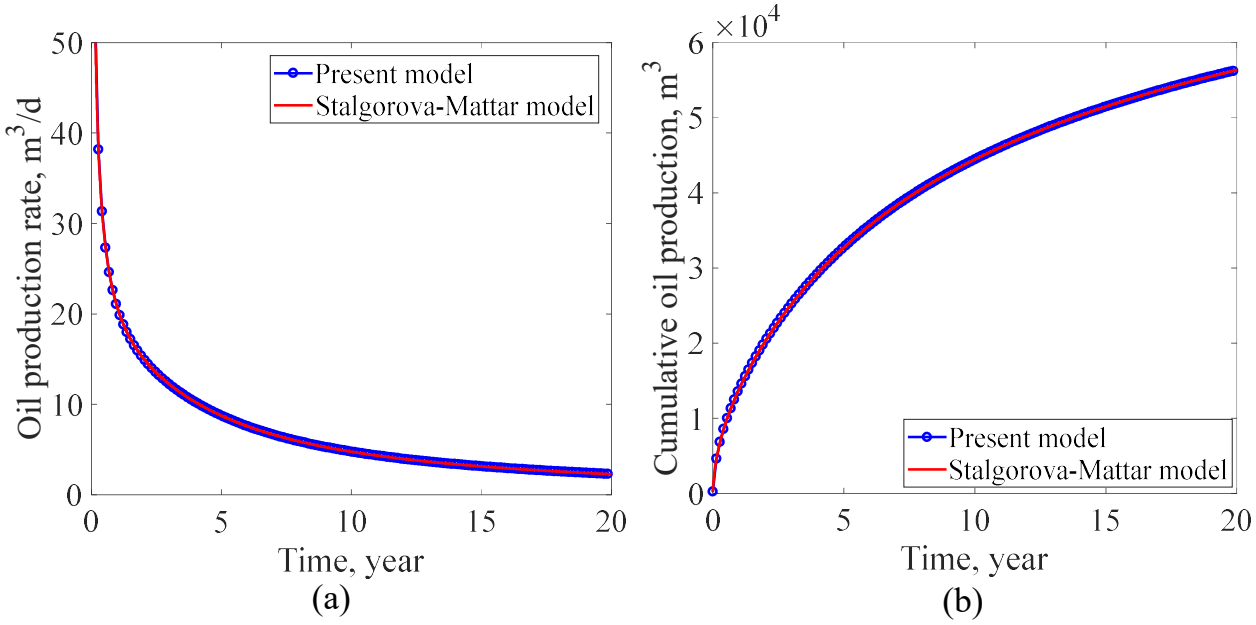


Figure 2. Comparison of results from the present simplified model with those from the Stalgorova–Mattar model [25]. (**a**) The variation in oil production rate with time. (**b**) The variation in cumulative oil production with time.

4.2. Sensitivity Analysis

The proposed model is employed to predict the oil production rate and cumulative oil production of shale oil wells operating under a constant bottomhole pressure. The parameters employed in the model are presented in Table 2. The PVT properties of oil and gas are shown in Figure 3, and the relative permeability curve is illustrated in Figure 4.

Table 2. Basic parameters used in the mathematical model for sensitivity analysis.

Parameters	Value	Unit
Porosity of the unstimulated reservoir (Regions 1, 2, and 3)	0.1	fraction
Initial permeability of the unstimulated reservoir (Regions 1, 2, and 3)	0.01	mD
Threshold pressure gradient of the unstimulated reservoir (Regions 1, 2, and 3)	0.005	MPa/m
Permeability modulus of the unstimulated reservoir (Regions 1, 2, and 3)	0.01	MPa^{-1}
Porosity of the stimulated reservoir (Region 4)	0.2	fraction
Initial permeability of the stimulated reservoir (Region 4)	1.0	mD

Table 2. *Cont.*

Parameters	Value	Unit
Threshold pressure gradient of the stimulated reservoir (Region 4)	0.001	MPa/m
Permeability modulus of the stimulated reservoir (Region 4)	0.05	MPa^{-1}
Porosity of the main fracture (Region 5)	0.2	fraction
Conductivity of the main fracture (Region 5)	5.0	$mD \cdot m$
Threshold pressure gradient of the main fracture (Region 5)	0.0001	MPa/m
Permeability modulus of the main fracture (Region 5)	0.05	MPa^{-1}
Initial reservoir pressure	15.8	MPa
Bubble point pressure	11.06	MPa
Bottomhole pressure	6.0	MPa
Initial water saturation	0.3	fraction
Reservoir thickness	14.5	m
Half-width of the reservoir	500	m
Number of main fractures	20	
Half-length of the main fracture	180	m
Width of the main fracture	0.02	m
Half-length of the stimulated reservoir for one main fracture	40	m
Half-length between main fractures	50	m

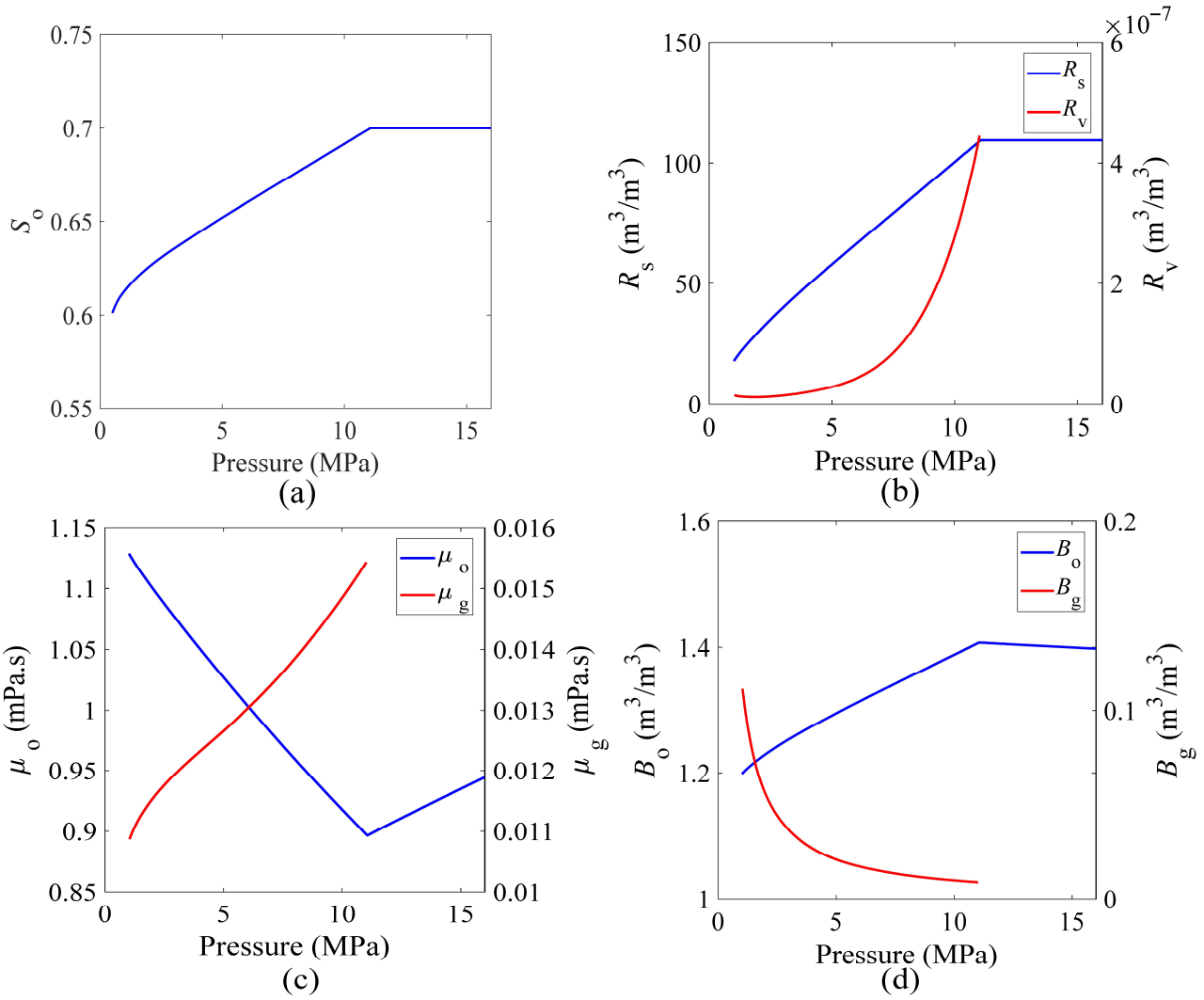


Figure 3. PVT properties of oil and gas. (**a**) Saturation–pressure relationship from CVD. (**b**) Solution gas–oil ratio and solution oil–gas ratio profiles. (**c**) Oil and gas viscosity profiles. (**d**) Oil and gas volume factor profiles.

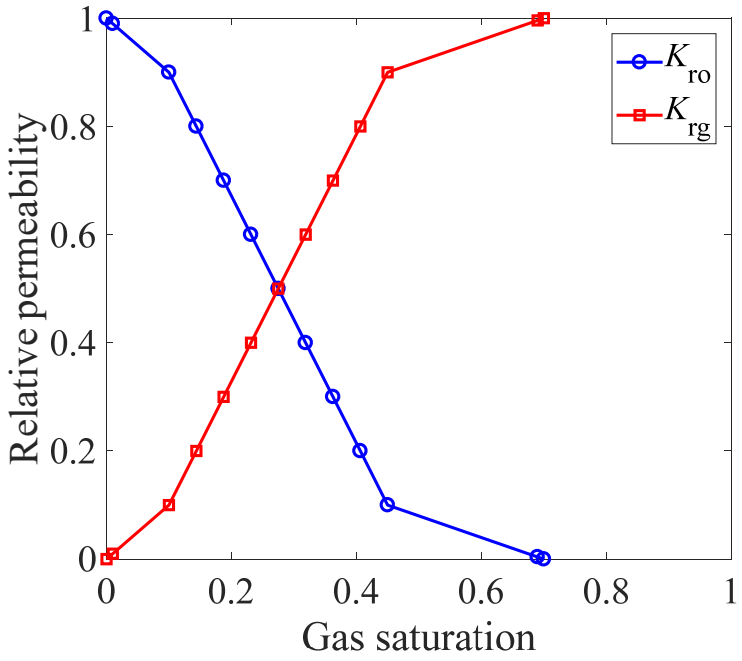


Figure 4. Relative permeability curves of oil and gas.

Figure 5 depicts the effect of the permeability modulus of the main fracture (γ_{o5}) on the oil production rate and cumulative oil production. As shown in Figure 5, the permeability modulus of the main fracture has a notable influence on both the oil production rate and cumulative oil production. Over time, the oil production rate declines sharply at first, after which the rate of decline slows; similarly, cumulative oil production increases rapidly initially and then more gradually. Furthermore, a higher permeability modulus results in a marked reduction in both the oil production rate and cumulative oil production. This is because an increased permeability modulus causes a rapid decline in the permeability of the main fracture, which results in a substantial reduction in oil production.

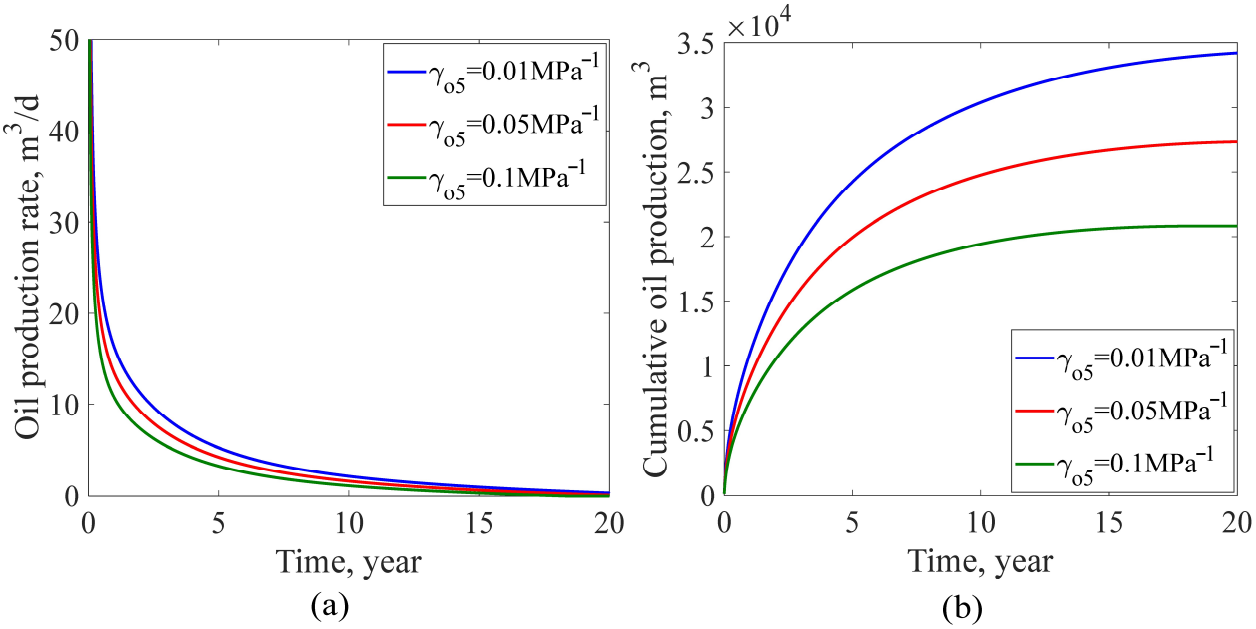


Figure 5. Effect of the permeability modulus of the main fracture (γ_{o5}) on the oil production rate and cumulative oil production. (**a**) The variation in oil production rate with time. (**b**) The variation in cumulative oil production with time.

Figure 6 illustrates the effect of the threshold pressure gradient of the main fracture (λ_{o5}) on the oil production rate and cumulative oil production. As shown in Figure 6, increasing the threshold pressure gradient leads to reductions in both the oil production rate and cumulative oil production. As the threshold pressure gradient increases, the oil production rate reaches zero at an earlier stage. This is because an increased threshold pressure gradient enhances the fluid's seepage resistance, leading to a reduction in the oil production rate. A higher threshold pressure gradient results in an earlier onset of conditions where the pressure difference falls below the threshold required for flow, thereby causing the oil production rate to reach zero at an earlier time.

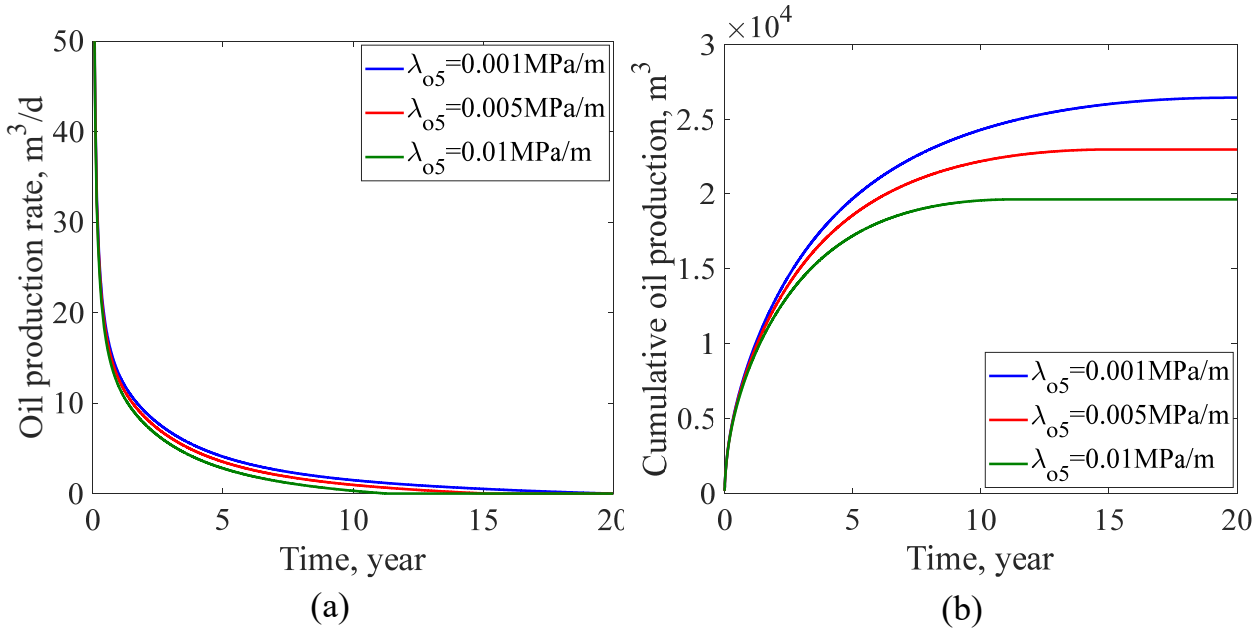


Figure 6. Effect of the threshold pressure gradient of the main fracture (λ_{o5}) on the oil production rate and cumulative oil production. (**a**) The variation in oil production rate with time. (**b**) The variation in cumulative oil production with time.

Figure 7 shows the effect of the conductivity of the main fracture (F_c) on the oil production rate and cumulative oil production. The conductivity of the main fracture is defined as the product of its width and permeability (i.e., $F_c = w_f \cdot K_{i5}$). As the conductivity of the main fracture increases, its permeability is enhanced, resulting in a higher initial oil production rate. However, the more rapid propagation of the pressure wave to the closed boundary consequently reduces the oil production rate during the intermediate and later stages. Despite this reduction, cumulative oil production continues to increase as the conductivity of the main fracture rises.

Figure 8 shows the effect of the half-length of the main fracture (y_1) on the oil production rate and cumulative oil production. As shown in Figure 8, an increase in the half-length of the main fracture leads to an increase in both the oil production rate and cumulative oil production. Interestingly, after ten years of production, when the pressure wave has reached the reservoir boundary, the half-length of the main fracture has a negligible effect on the oil production rate. This is because, during the early production period characterized by unstable flow, extending the half-length of the main fracture effectively increases the seepage pathways near the wellbore, thereby enhancing the oil production rate. In contrast, during the later pseudo-steady flow stage, the oil production rate becomes insensitive to further increases in fracture length.

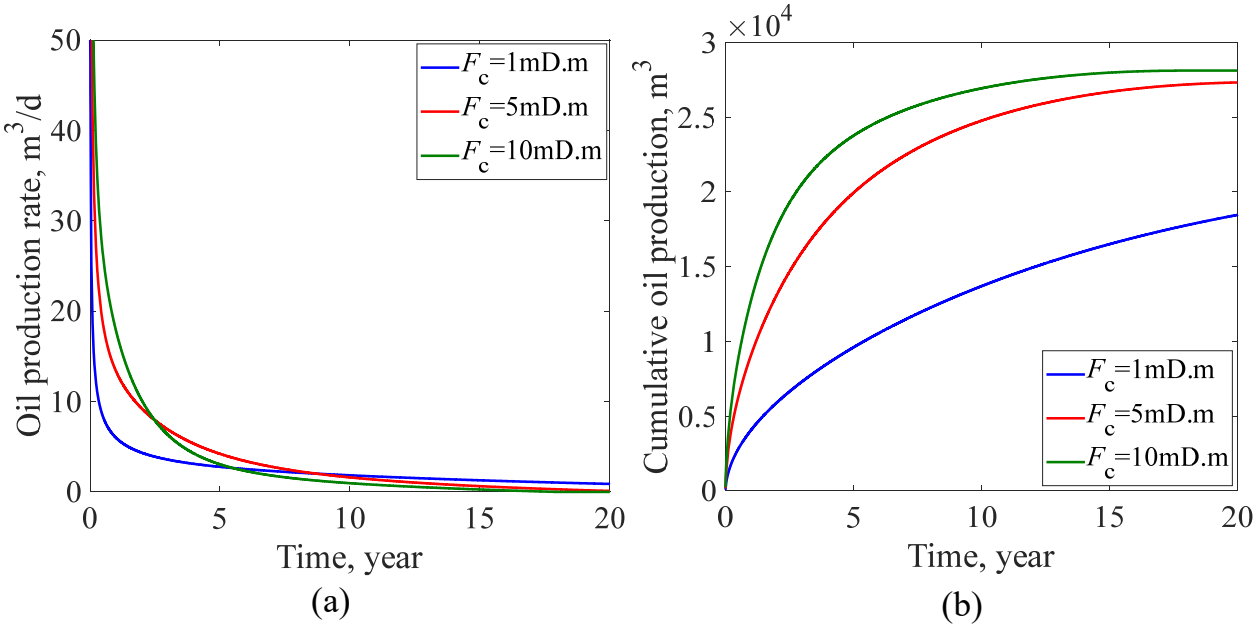


Figure 7. Effect of conductivity of the main fracture (F_c) on the oil production rate and cumulative oil production. (**a**) The variation in oil production rate with time. (**b**) The variation in cumulative oil production with time.

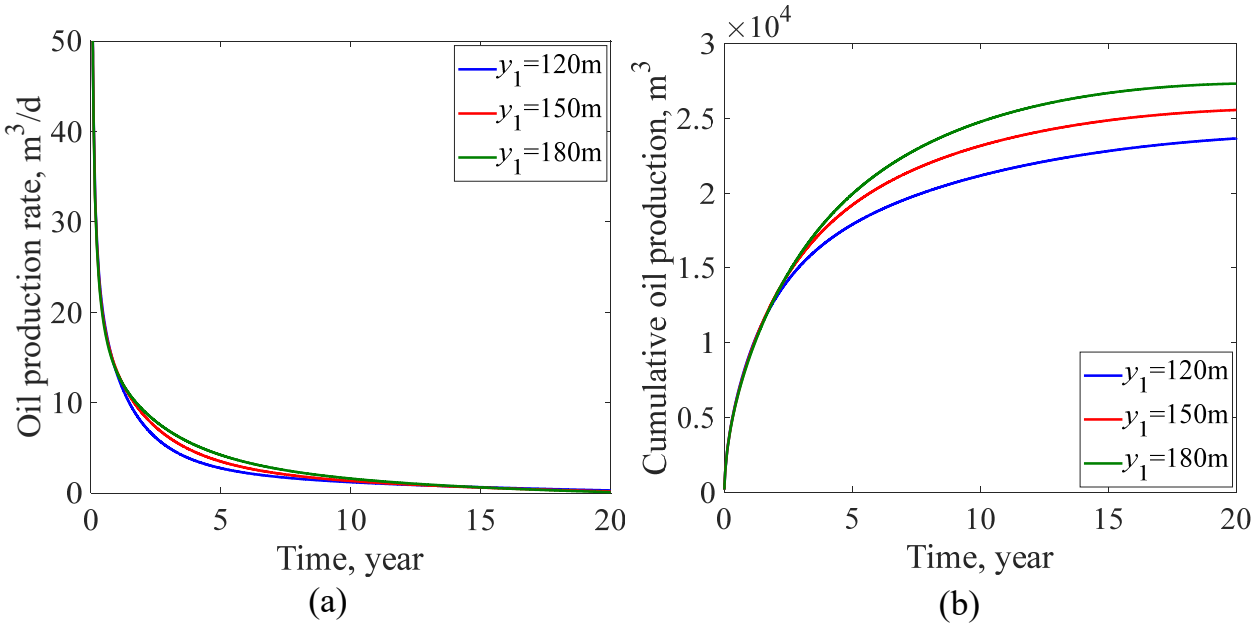


Figure 8. Effect of the half-length of the main fracture (y_1) on the oil production rate and cumulative oil production. (**a**) The variation in oil production rate with time. (**b**) The variation in cumulative oil production with time.

Figure 9 depicts the effect of the half-width of the reservoir (y_2) on the oil production rate and cumulative oil production. As illustrated in Figure 9, the half-width of the reservoir influences the oil production rate and cumulative oil production only after the pressure wave reaches the closed reservoir boundary. As the half-width of the reservoir decreases, both the oil production rate and cumulative oil production decline. This phenomenon occurs because reducing the half-width of the reservoir causes the pressure wave to reach the boundary earlier, thereby diminishing both the oil production rate and cumulative oil production.

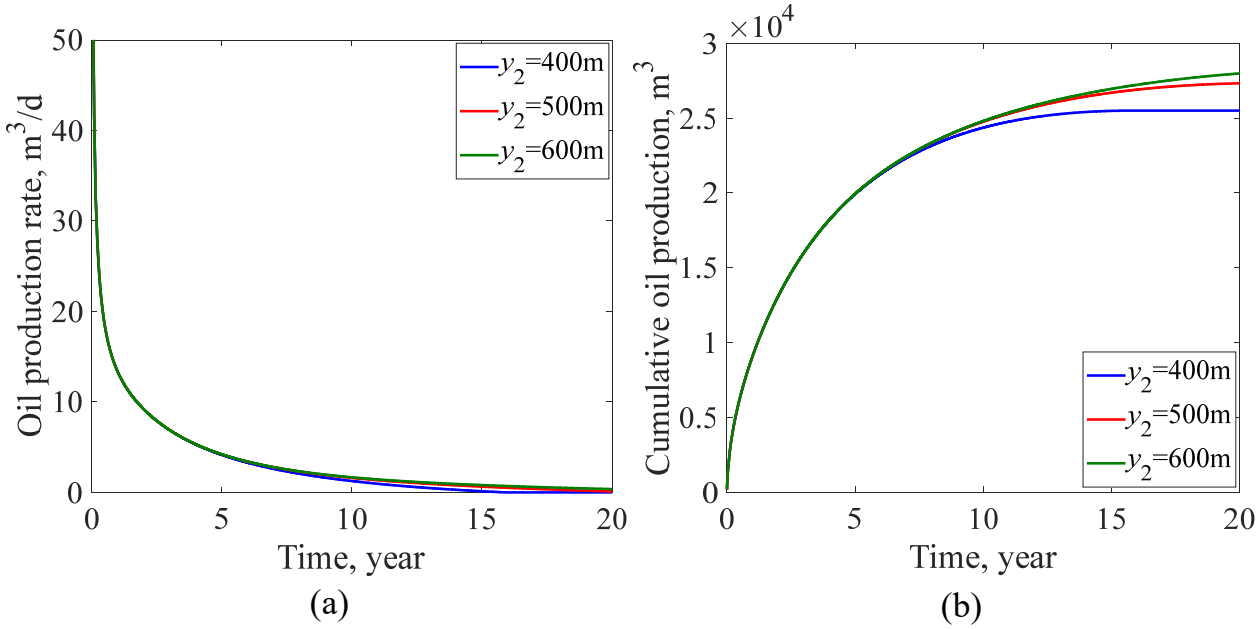


Figure 9. Effect of the half-width of the reservoir (y_2) on the oil production rate and cumulative oil production. (**a**) The variation in oil production rate with time. (**b**) The variation in cumulative oil production with time.

Figure 10 illustrates the effect of the threshold pressure gradient of the unstimulated reservoir ($\lambda_{o1}, \lambda_{o2}, \lambda_{o3}$) on the oil production rate and cumulative oil production. As shown in Figure 10, as the threshold pressure gradient of the unstimulated reservoir increases, fluid flow must overcome greater seepage resistance, leading to a reduction in both the oil production rate and cumulative oil production. When the threshold pressure gradient exceeds the displacement pressure difference within the reservoir, the oil production rate ceases entirely. Consequently, by increasing the threshold pressure gradient, the time required for the oil production rate to decline to zero decreases.

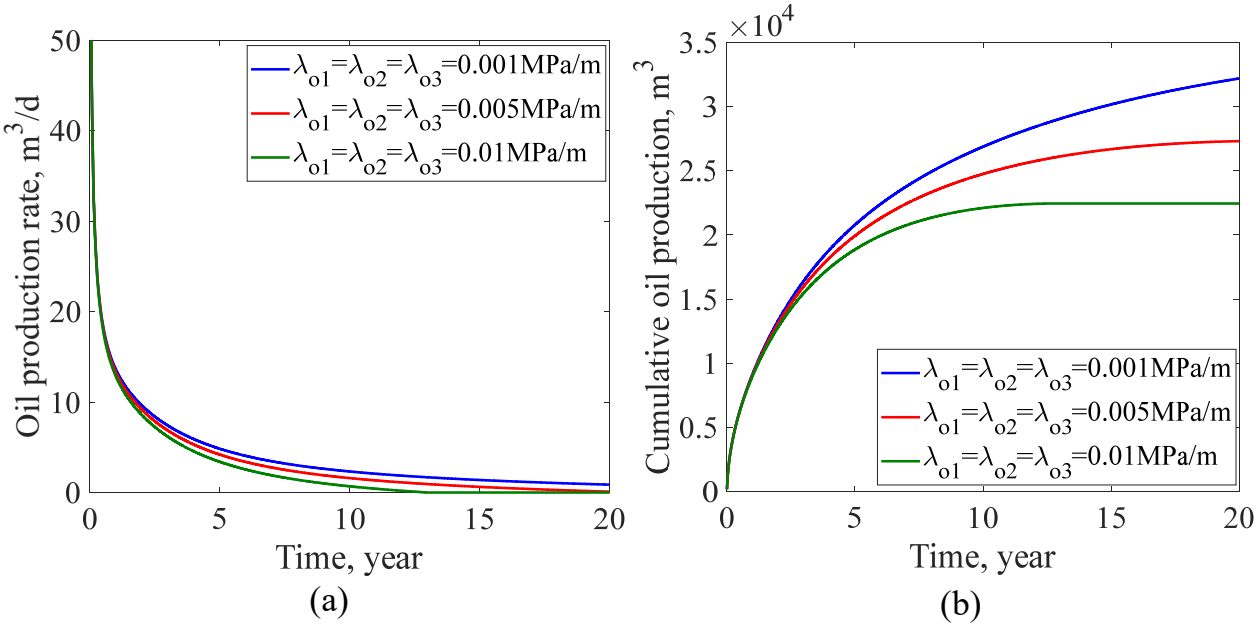


Figure 10. Effect of the threshold pressure gradient of the unstimulated reservoir (λ_{o1}, λ_{o2}, λ_{o3}) on the oil production rate and cumulative oil production. (**a**) The variation in oil production rate with time. (**b**) The variation in cumulative oil production with time.

Figure 11 illustrates the effect of the threshold pressure gradient of the stimulated reservoir (λ_{o4}) on the oil production rate and cumulative oil production. Evidently, a higher threshold pressure gradient of the stimulated reservoir leads to a decline in both the oil production rate and cumulative oil production. Compared to the threshold pressure gradient of the unstimulated reservoir, that of the stimulated reservoir has a smaller influence on both the oil production rate and cumulative oil production. This is likely due to the fact that the threshold pressure gradient of the stimulated reservoir has a relatively limited effect on the overall seepage capacity of the reservoir compared to that of the unstimulated reservoir.

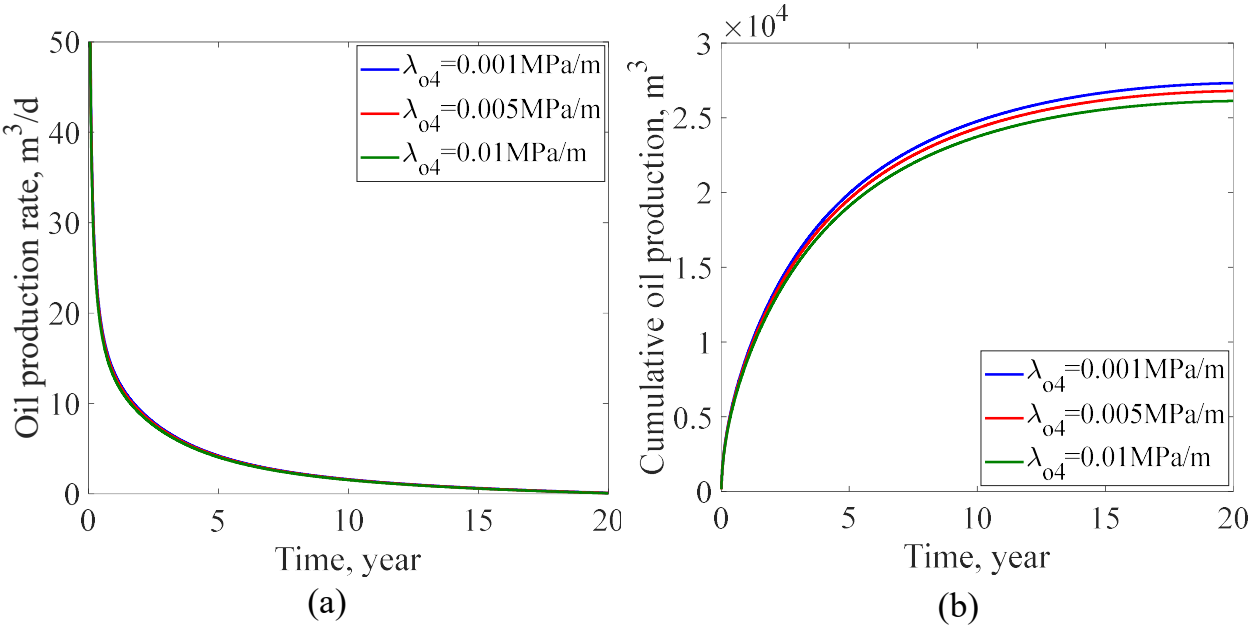


Figure 11. Effect of the threshold pressure gradient of the stimulated reservoir (λ_{o4}) on the oil production rate and cumulative oil production. (**a**) The variation in oil production rate with time. (**b**) The variation in cumulative oil production with time.

4.3. Field Data Analysis

The field example is from a shale formation in the Ordos Basin of China. The PVT properties and relative permeability curve are shown in Figures 3 and 4, respectively. A horizontal well is hydraulically fractured in 22 stages, with an average fracture half-length of 180 m. The threshold pressure gradients of the unstimulated reservoir, stimulated reservoir, and main fracture are 0.0002, 0.0001, and 0.0001MPa/m, respectively. The permeability modules of the unstimulated reservoir, stimulated reservoir, and main fracture are 0.0005, 0.001, and 0.001 MPa^{-1}, respectively. The porosities of the unstimulated reservoir, stimulated reservoir, and main fracture are 0.15, 0.2, and 0.3, respectively. The initial permeabilities of the unstimulated reservoir and stimulated reservoir are 0.2 and 4.0 mD, respectively. The conductivity of the main fracture is 7.0 mD · m. The remaining parameters are consistent with those presented in Table 2. The proposed analytical model is applied to analyze the field production data of the multi-fractured horizontal well. In the actual field scenario, the bottomhole pressure is prone to fluctuations due to various well operations. Therefore, Duhamel's principle is utilized to analyze the production data under variable bottomhole pressure conditions [55]. As depicted in Figure 12, we present the field production data alongside our predicted production results. Evidently, our model demonstrates an excellent match with the production data. Furthermore, the proposed model can predict the oil production rate and cumulative oil production over a 20-year period under the current bottomhole pressure conditions, thereby enabling the evaluation

of shale oil well productivity. The 20-year cumulative oil production volume of this well is 23,669 m^3. This case effectively validates the applicability and practical usefulness of the proposed analytical model.

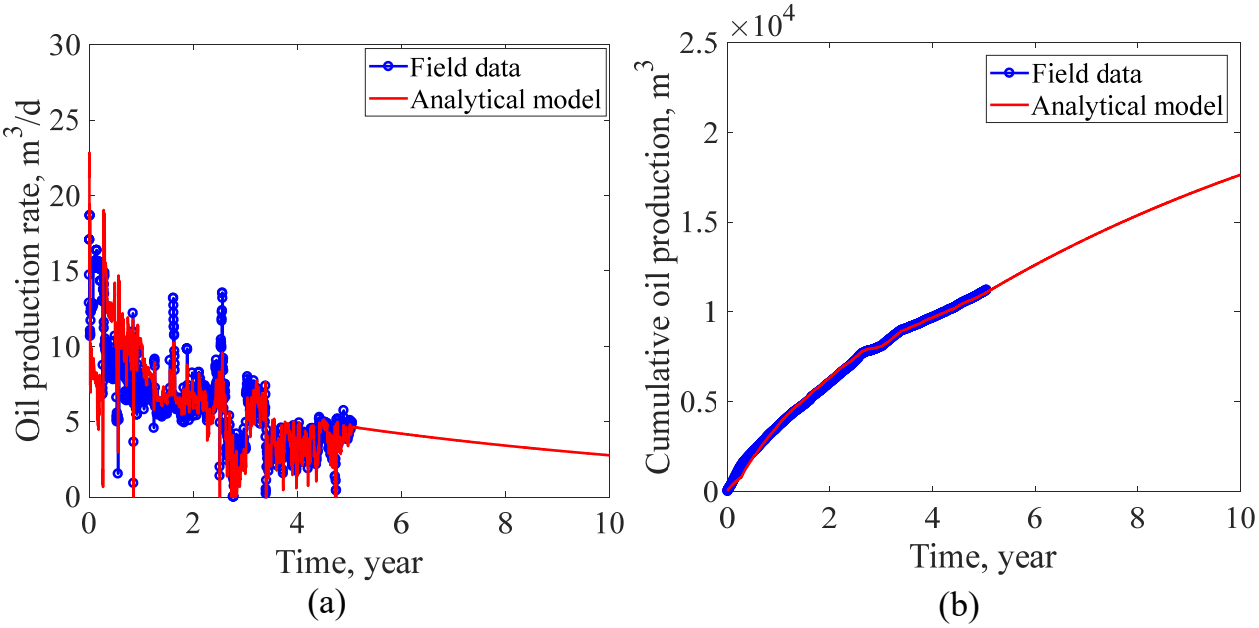


Figure 12. History matching results for the field case. (**a**) The variation in oil production rate with time. (**b**) The variation in cumulative oil production with time.

4.4. Sensitivity to Input Data Errors

Finally, we examine the sensitivity of the present model to errors in the input data. The basic parameters in the model are identical to those presented in Table 2. The model is employed to forecast the 20-year cumulative oil production period under a constant bottomhole pressure. To assess the impact of parameter inaccuracies on the 20-year cumulative oil production forecast, we introduce input values that deviate from the correct parameters by relative errors of 50% and 100%, respectively. The effect of input data inaccuracies on the relative error in the 20-year cumulative oil production prediction is shown in Table 3. Clearly, the influence of input parameter errors on prediction results is not uniform and varies significantly across different parameters. Among them, the permeability modulus of the main fracture, the half-length of the main fracture, and the threshold pressure gradient of the unstimulated reservoir exhibit relatively higher sensitivity to input inaccuracies, thereby having a more pronounced effect on prediction accuracy. Specifically, when the relative error in the permeability modulus of the main fracture reaches 50% and 100%, the corresponding errors in the prediction results increase to 12.85% and 23.77%, respectively. For the half-length of the main fracture, the same levels of input error lead to prediction errors of 13.60% and 16.65%, respectively, while for the threshold pressure gradient of the unstimulated reservoir, the resulting prediction errors are 10.14% and 17.78%, respectively. These results indicate that the magnitude of the input error directly correlates with a degradation in prediction performance, particularly for these three parameters.

Furthermore, the threshold pressure gradient of the main fracture and that of the stimulated reservoir exhibit minimal sensitivity to input errors, resulting in only a slight degradation in prediction accuracy. Specifically, when the relative error in the threshold pressure gradient of the main fracture reaches 50% and 100%, the corresponding prediction errors are only 0.18% and 0.36%, respectively. Similarly, for the threshold pressure gradient of the stimulated reservoir, input errors of 50% and 100% lead to prediction errors of 0.24%

and 0.48%, respectively. These negligible changes indicate that the prediction model is highly robust against inaccuracies in these two parameters.

In contrast, the conductivity of the main fracture and the half-width of the reservoir demonstrate moderate sensitivity to input parameter errors, leading to an intermediate level of influence on prediction accuracy. Specifically, when the relative error in the conductivity of the main fracture reaches 50% and 100%, the corresponding prediction errors are 2.08% and 2.90%, respectively. Similarly, for the half-width of the reservoir, input errors of 50% and 100% result in prediction errors of 3.03% and 3.04%, respectively. These results suggest that while inaccuracies in these parameters do affect the model output, the effect is significantly less pronounced than that observed for highly sensitive parameters yet more notable than for those with a negligible impact.

Table 3. Impact of input data inaccuracies on relative error in the 20-year cumulative oil production prediction.

Input Data			20-Year Cumulative Oil Production	
Parameter	**Value (Unit)**	**Relative Error**	**Value (Unit)**	**Relative Error**
Permeability modulus of the main fracture (γ_{o5})	0.05 (MPa^{-1})	0%	27,323 (m^3)	0%
	0.075 (MPa^{-1})	50%	23,813 (m^3)	12.85%
	0.1 (MPa^{-1})	100%	20,830 (m^3)	23.77%
Threshold pressure gradient of the main fracture (λ_{o5})	0.0001 (MPa/m)	0%	27,323 (m^3)	0%
	0.00015 (MPa/m)	50%	27,274 (m^3)	0.18%
	0.0002 (MPa/m)	100%	27,225 (m^3)	0.36%
Conductivity of the main fracture (F_c)	5.0 (mD·m)	0%	27,323 (m^3)	0%
	7.5 (mD·m)	50%	27,891 (m^3)	2.08%
	10.0 (mD·m)	100%	28,115 (m^3)	2.90%
Half-length of the main fracture (y_1)	180 (m)	0%	27,323 (m^3)	0%
	270 (m)	50%	31,039 (m^3)	13.60%
	360 (m)	100%	31,872 (m^3)	16.65%
Half-width of the reservoir (y_2)	500 (m)	0%	27,323 (m^3)	0%
	750 (m)	50%	28,150 (m^3)	3.03%
	1000 (m)	100%	28,154 (m^3)	3.04%
Threshold pressure gradient of the unstimulated reservoir (λ_{o1}, λ_{o2}, and λ_{o3})	0.005 (MPa/m)	0%	27,323 (m^3)	0%
	0.0075 (MPa/m)	50%	24,553 (m^3)	10.14%
	0.01 (MPa/m)	100%	22,465 (m^3)	17.78%
Threshold pressure gradient of the stimulated reservoir (λ_{o4})	0.001 (MPa/m)	0%	27,323 (m^3)	0%
	0.0015 (MPa/m)	50%	27,257 (m^3)	0.24%
	0.002 (MPa/m)	100%	27,191 (m^3)	0.48%

5. Conclusions

The principal contribution of this study is the development of an analytical model for analyzing production data and forecasting shale oil well performance while taking into account multiphase flow, threshold pressure gradients, and stress sensitivity. Pedrosa's transformation, perturbation theory, the Laplace transform, and the Stehfest numerical inversion method are employed to solve the proposed model. A comprehensive investigation of the production characteristics of shale oil wells is conducted, and the impacts of key parameters on the oil production rate and cumulative oil production are thoroughly discussed. A field case study is presented to demonstrate the application and effectiveness of the proposed analytical model.

It has been observed that an increase in the permeability modulus of the main fracture results in significant decreases in both the oil production rate and cumulative oil production. A 100% increase in the permeability modulus of the main fracture results in a 23.77% reduction in 20-year cumulative oil production. Similarly, an increase in the threshold pressure gradient of the main fracture leads to reductions in these production metrics, and a higher threshold pressure gradient causes the oil production rate to reach zero earlier. However, a 100% increase in the threshold pressure gradient of the main fracture results in only a 0.36% decrease in 20-year cumulative oil production. Moreover, an increase in the conductivity of the main fracture enhances its permeability, thereby increasing the initial oil production rate while reducing the production rate in the later stages. When the conductivity of the main fracture increases by 100%, the 20-year cumulative oil production increases by 2.90%. In addition, a decrease in reservoir half-width allows the pressure wave to reach the boundary sooner, diminishing both the oil production rate and cumulative oil production. An increase in the reservoir half-width by 100% results in a 3.04% increase in 20-year cumulative oil production. Finally, a higher threshold pressure gradient of the stimulated reservoir leads to declines in both the oil production rate and cumulative oil production; however, its effect is less pronounced compared to that of the unstimulated reservoir. A 100% increase in the threshold pressure gradient of the stimulated reservoir results in only a 0.48% rise in 20-year cumulative oil production, whereas the same increase in the threshold pressure gradient of the unstimulated reservoir leads to a 17.78% increase in 20-year cumulative oil production.

The proposed analytical model provides an efficient and practical approach for analyzing production data and forecasting shale oil well performance. In contrast to previous models, this model comprehensively accounts for the impacts of factors such as multiphase flow, threshold pressure gradients, and stress sensitivity, thereby aligning more closely with actual field conditions. Consequently, it has a wider range of potential applications.

Author Contributions: Conceptualization, Z.L.; Methodology, Z.L., X.Y. and J.R.; Validation, Z.L.; Formal analysis, K.X. and Y.S.; Investigation, Z.L., X.Y. and J.R.; Data curation, Y.S.; Writing—original draft, Z.L., K.X. and X.Y.; Writing—review & editing, P.G. and J.R.; Visualization, K.X. and J.R.; Supervision, P.G.; Project administration, P.G. and J.R.; Funding acquisition, Z.L. All authors have read and agreed to the published version of the manuscript.

Funding: This research was funded by the National Science and Technology Major Project (No. 2025ZD1404800), the Major Applied Science and Technology Special Project of PetroChina Company (No. 2023ZZ15YJ03), and the Major Special Project of PetroChina Changqing Oilfield Company (No. 2023DZZ04).

Data Availability Statement: The original contributions presented in the study are included in the article, further inquiries can be directed to the corresponding author.

Conflicts of Interest: Authors Zhen Li, Kai Xu and Yuyi Shen were employed by the company PetroChina Changqing Oilfield Company. The remaining authors declare that the research was conducted in the absence of any commercial or financial relationships that could be construed as a potential conflict of interest.

Appendix A

Appendix A.1. Region 1

After substituting Equations (27) and (28) into Equations (4) and (7)–(9), the zeroth-order equations for Region 1 are obtained as follows:

$$\begin{cases} \frac{\partial^2 \tau_{o01}}{\partial y^2} - G_{o1} \frac{\partial \tau_{o01}}{\partial y} = \frac{\phi_1 \eta_{o1}}{CK_{i1}} \frac{\partial \tau_{o01}}{\partial t}, \\ \tau_{o01}\big|_{t=0} = 0, \\ \left.\frac{\partial \tau_{o01}}{\partial y}\right|_{y=y_2} = 0, \\ \tau_{o01}\big|_{y=y_1} = \tau_{o04}\big|_{y=y_1}. \end{cases} \tag{A1}$$

The Laplace transform is introduced to analytically solve Equation (A1). Taking the Laplace transform of Equation (A1) with respect to t, one can obtain

$$\begin{cases} \frac{\partial^2 \overline{\tau}_{o01}}{\partial y^2} - G_{o1} \frac{\partial \overline{\tau}_{o01}}{\partial y} = \frac{\phi_1 \eta_{o1}}{CK_{i1}} s\overline{\tau}_{o01}, \\ \left.\frac{\partial \overline{\tau}_{o01}}{\partial y}\right|_{y=y_2} = 0, \\ \overline{\tau}_{o01}\big|_{y=y_1} = \overline{\tau}_{o04}\big|_{y=y_1}. \end{cases} \tag{A2}$$

Subsequently, the analytical solution of Equation (A2) can be derived as follows:

$$\overline{\tau}_{o01} = \frac{A_2 e^{A_1(y-y_2)} - A_1 e^{A_2(y-y_2)}}{A_2 e^{A_1(y_1-y_2)} - A_1 e^{A_2(y_1-y_2)}} \overline{\tau}_{o04}\big|_{y=y_1}, \tag{A3}$$

where

$$A_1 = \frac{G_{o1} + \sqrt{G_{o1}^2 + \frac{4\phi_1 \eta_{o1} s}{CK_{i1}}}}{2}, \tag{A4}$$

$$A_2 = \frac{G_{o1} - \sqrt{G_{o1}^2 + \frac{4\phi_1 \eta_{o1} s}{CK_{i1}}}}{2}. \tag{A5}$$

Appendix A.2. Region 2

By substituting Equations (27) and (28) into Equations (10)–(13), we obtain the following zeroth-order equations for Region 2:

$$\begin{cases} \frac{\partial^2 \tau_{o02}}{\partial y^2} - G_{o2} \frac{\partial \tau_{o02}}{\partial y} = \frac{\phi_2 \eta_{o2}}{CK_{i2}} \frac{\partial \tau_{o02}}{\partial t}, \\ \tau_{o02}\big|_{t=0} = 0, \\ \left.\frac{\partial \tau_{o02}}{\partial y}\right|_{y=y_2} = 0, \\ \tau_{o02}\big|_{y=y_1} = \tau_{o03}\big|_{y=y_1}. \end{cases} \tag{A6}$$

Taking the Laplace transform of Equation (A6) with respect to t, we obtain the following results:

$$\begin{cases} \frac{\partial^2 \overline{\tau}_{o02}}{\partial y^2} - G_{o2} \frac{\partial \overline{\tau}_{o02}}{\partial y} = \frac{\phi_2 \eta_{o2}}{CK_{i2}} s\overline{\tau}_{o02}, \\ \left.\frac{\partial \overline{\tau}_{o02}}{\partial y}\right|_{y=y_2} = 0, \\ \overline{\tau}_{o02}\big|_{y=y_1} = \overline{\tau}_{o03}\big|_{y=y_1}. \end{cases} \tag{A7}$$

By solving Equation (A7), the analytical solution can be derived as follows:

$$\overline{\tau}_{o02} = \frac{B_2 e^{B_1(y-y_2)} - B_1 e^{B_2(y-y_2)}}{B_2 e^{B_1(y_1-y_2)} - B_1 e^{B_2(y_1-y_2)}} \overline{\tau}_{o03}, \tag{A8}$$

where

$$B_1 = \frac{G_{o2} + \sqrt{G_{o2}^2 + \frac{4\phi_2 \eta_{o2} s}{CK_{i2}}}}{2}, \tag{A9}$$

$$B_2 = \frac{G_{o2} - \sqrt{G_{o2}^2 + \frac{4\phi_2 \eta_{o2} s}{CK_{i2}}}}{2}. \tag{A10}$$

Appendix A.3. Region 3

By substituting Equations (27) and (28) into Equations (14)–(17), we derive the zeroth-order equations for Region 3 as follows:

$$\begin{cases} \frac{\partial^2 \tau_{o03}}{\partial x^2} - G_{o3}\frac{\partial \tau_{o03}}{\partial x} + \frac{1}{y_1}\frac{K_{i2}}{K_{i3}}\left[\frac{\partial \tau_{o02}}{\partial y} + (1-\gamma_{o2}\tau_{o02})\left(\frac{K_{ro}}{\mu_o B_o} + R_v\frac{K_{rg}}{\mu_g B_g}\right)\lambda_2\right]\Big|_{y=y_1} = \frac{\phi_3\eta_{o3}}{CK_{i3}}\frac{\partial \tau_{o03}}{\partial t}, \\ \tau_{o03}|_{t=0} = 0, \\ \frac{\partial \tau_{o03}}{\partial x}\Big|_{x=x_2} = 0, \\ \tau_{o03}|_{x=x_1} = \tau_{o04}|_{x=x_1}. \end{cases} \tag{A11}$$

Taking the Laplace transform of Equation (A11) with respect to t yields

$$\begin{cases} \frac{\partial^2 \overline{\tau}_{o03}}{\partial x^2} - G_{o3}\frac{\partial \overline{\tau}_{o03}}{\partial x} + \frac{1}{y_1}\frac{K_{i2}}{K_{i3}}\left[\frac{\partial \overline{\tau}_{o02}}{\partial y} + \left(\frac{1}{s}-\gamma_{o2}\overline{\tau}_{o02}\right)\left(\frac{K_{ro}}{\mu_o B_o} + R_v\frac{K_{rg}}{\mu_g B_g}\right)\lambda_2\right]\Big|_{y=y_1} = \frac{\phi_3\eta_{o3}}{CK_{i3}}s\overline{\tau}_{o03}, \\ \frac{\partial \overline{\tau}_{o03}}{\partial x}\Big|_{x=x_2} = 0, \\ \overline{\tau}_{o03}|_{x=x_1} = \overline{\tau}_{o04}|_{x=x_1}. \end{cases} \tag{A12}$$

Based on Equation (A8), Equation (A12) can be reformulated as follows:

$$\begin{cases} \frac{\partial^2 \overline{\tau}_{o03}}{\partial x^2} - G_{o3}\frac{\partial \overline{\tau}_{o03}}{\partial x} - f_3(s)\overline{\tau}_{o03} = g_3(s), \\ \frac{\partial \overline{\tau}_{o03}}{\partial x}\Big|_{x=x_2} = 0, \\ \overline{\tau}_{o03}|_{x=x_1} = \overline{\tau}_{o04}|_{x=x_1}, \end{cases} \tag{A13}$$

where

$$f_3(s) = \frac{\phi_3\eta_{o3}s}{CK_{i3}} - \frac{1}{y_1}\frac{K_{i2}}{K_{i3}}\left[\beta_2 - \gamma_{o2}\left(\frac{K_{ro}}{\mu_o B_o} + R_v\frac{K_{rg}}{\mu_g B_g}\right)\lambda_2\right], \tag{A14}$$

$$g_3(s) = -\frac{1}{y_1}\frac{K_{i2}}{K_{i3}}\frac{1}{s}\left(\frac{K_{ro}}{\mu_o B_o} + R_v\frac{K_{rg}}{\mu_g B_g}\right)\lambda_2, \tag{A15}$$

$$\beta_2 = \frac{B_1 B_2 e^{B_1(y_1-y_2)} - B_1 B_2 e^{B_2(y_1-y_2)}}{B_2 e^{B_1(y_1-y_2)} - B_1 e^{B_2(y_1-y_2)}}. \tag{A16}$$

By solving Equation (A13), we obtain the following analytical solution:

$$\overline{\tau}_{o03} = \frac{C_2 e^{C_1(x-x_2)} - C_1 e^{C_2(x-x_2)}}{C_2 e^{C_1(x_1-x_2)} - C_1 e^{C_2(x_1-x_2)}}\left[\frac{g_3(s)}{f_3(s)} + \overline{\tau}_{o04}|_{x=x_1}\right] - \frac{g_3(s)}{f_3(s)}, \tag{A17}$$

where

$$C_1 = \frac{G_{o3} + \sqrt{G_{o3}^2 + 4f_3(s)}}{2}, \tag{A18}$$

$$C_2 = \frac{G_{o3} - \sqrt{G_{o3}^2 + 4f_3(s)}}{2}. \tag{A19}$$

Appendix A.4. Region 4

By substituting Equations (27) and (28) into Equations (18)–(21), we obtain the zeroth-order equations for Region 4 as follows:

$$\begin{cases} \frac{\partial^2 \tau_{o04}}{\partial x^2} - G_{o4}\frac{\partial \tau_{o04}}{\partial x} + \frac{1}{y_1}\frac{K_{i1}}{K_{i4}}\left[\frac{\partial \tau_{o01}}{\partial y} + (1-\gamma_{o1}\tau_{o01})\left(\frac{K_{ro}}{\mu_o B_o} + R_v\frac{K_{rg}}{\mu_g B_g}\right)\lambda_1\right]\Big|_{y=y_1} = \frac{\phi_4\eta_{o4}}{CK_{i4}}\frac{\partial \tau_{o04}}{\partial t}, \\ \tau_{o04}|_{t=0} = 0, \\ K_{i3}\left[\frac{\partial \tau_{o03}}{\partial x} + (1-\gamma_{o3}\tau_{o03})\left(\frac{K_{ro}}{\mu_o B_o} + R_v\frac{K_{rg}}{\mu_g B_g}\right)\lambda_3\right]\Big|_{x=x_1} \\ = K_{i4}\left[\frac{\partial \tau_{o04}}{\partial x} + (1-\gamma_{o4}\tau_{o04})\left(\frac{K_{ro}}{\mu_o B_o} + R_v\frac{K_{rg}}{\mu_g B_g}\right)\lambda_4\right]\Big|_{x=x_1}, \\ \tau_{o04}|_{x=\frac{w_f}{2}} = \tau_{o05}|_{x=\frac{w_f}{2}}. \end{cases} \tag{A20}$$

By applying the Laplace transform to Equation (A20) with respect to t, we obtain the following expression:

$$\begin{cases} \frac{\partial^2 \overline{\tau}_{o04}}{\partial x^2} - G_{o4}\frac{\partial \overline{\tau}_{o04}}{\partial x} + \frac{1}{y_1}\frac{K_{i1}}{K_{i4}}\left[\frac{\partial \overline{\tau}_{o01}}{\partial y} + \left(\frac{1}{s}-\gamma_{o1}\overline{\tau}_{o01}\right)\left(\frac{K_{ro}}{\mu_o B_o} + R_v\frac{K_{rg}}{\mu_g B_g}\right)\lambda_1\right]\Big|_{y=y_1} = \frac{\phi_4\eta_{o4}}{CK_{i4}}s\overline{\tau}_{o04}, \\ K_{i3}\left[\frac{\partial \overline{\tau}_{o03}}{\partial x} + \left(\frac{1}{s}-\gamma_{o3}\overline{\tau}_{o03}\right)\left(\frac{K_{ro}}{\mu_o B_o} + R_v\frac{K_{rg}}{\mu_g B_g}\right)\lambda_3\right]\Big|_{x=x_1} \\ = K_{i4}\left[\frac{\partial \overline{\tau}_{o04}}{\partial x} + \left(\frac{1}{s}-\gamma_{o4}\overline{\tau}_{o04}\right)\left(\frac{K_{ro}}{\mu_o B_o} + R_v\frac{K_{rg}}{\mu_g B_g}\right)\lambda_4\right]\Big|_{x=x_1}, \\ \overline{\tau}_{o04}|_{x=\frac{w_f}{2}} = \overline{\tau}_{o05}|_{x=\frac{w_f}{2}}. \end{cases} \tag{A21}$$

Based on Equations (A3) and (A17), Equation (A21) can be rewritten as follows:

$$\begin{cases} \frac{\partial^2 \overline{\tau}_{o04}}{\partial x^2} - G_{o4}\frac{\partial \overline{\tau}_{o04}}{\partial x} - f_4(s)\overline{\tau}_{o04} = g_4(s), \\ K_{i3}\left[\beta_3\left(\frac{g_3(s)}{f_3(s)} + \overline{\tau}_{o04}\right) + \left(\frac{1}{s}-\gamma_{o3}\overline{\tau}_{o04}\right)\left(\frac{K_{ro}}{\mu_o B_o} + R_v\frac{K_{rg}}{\mu_g B_g}\right)\lambda_3\right]\Big|_{x=x_1} \\ = K_{i4}\left[\frac{\partial \overline{\tau}_{o04}}{\partial x} + \left(\frac{1}{s}-\gamma_{o4}\overline{\tau}_{o04}\right)\left(\frac{K_{ro}}{\mu_o B_o} + R_v\frac{K_{rg}}{\mu_g B_g}\right)\lambda_4\right]\Big|_{x=x_1}, \\ \overline{\tau}_{o04}|_{x=\frac{w_f}{2}} = \overline{\tau}_{o05}|_{x=\frac{w_f}{2}}, \end{cases} \tag{A22}$$

where

$$f_4(s) = \frac{\phi_4\eta_{o4}s}{CK_{i4}} - \frac{1}{y_1}\frac{K_{i1}}{K_{i4}}\left[\beta_1 - \gamma_{o1}\left(\frac{K_{ro}}{\mu_o B_o} + R_v\frac{K_{rg}}{\mu_g B_g}\right)\lambda_1\right], \tag{A23}$$

$$g_4(s) = -\frac{1}{y_1}\frac{K_{i1}}{K_{i4}}\frac{1}{s}\left(\frac{K_{ro}}{\mu_o B_o} + R_v\frac{K_{rg}}{\mu_g B_g}\right)\lambda_1, \tag{A24}$$

$$\beta_1 = \frac{A_1A_2e^{A_1(y_1-y_2)} - A_1A_2e^{A_2(y_1-y_2)}}{A_2e^{A_1(y_1-y_2)} - A_1e^{A_2(y_1-y_2)}}, \tag{A25}$$

$$\beta_3 = \frac{C_1C_2e^{C_1(x_1-x_2)} - C_1C_2e^{C_2(x_1-x_2)}}{C_2e^{C_1(x_1-x_2)} - C_1e^{C_2(x_1-x_2)}}. \tag{A26}$$

By solving Equation (A22), we derive the following analytical solution:

$$\begin{aligned} \overline{\tau}_{o04} = {} & \frac{\left(\overline{\tau}_{o05} + \frac{g_4(s)}{f_4(s)}\right)\left\{\left[D_2 - \gamma_{o4}\xi_{o4} - \frac{K_{i3}}{K_{i4}}(\beta_3 - \gamma_{o3}\xi_{o3})\right]e^{D_1(x-x_1)} - \left[D_1 - \gamma_{o4}\xi_{o4} - \frac{K_{i3}}{K_{i4}}(\beta_3 - \gamma_{o3}\xi_{o3})\right]e^{D_2(x-x_1)}\right\}}{\left[D_2 - \gamma_{o4}\xi_{o4} - \frac{K_{i3}}{K_{i4}}(\beta_3 - \gamma_{o3}\xi_{o3})\right]e^{D_1(\frac{w_f}{2}-x_1)} - \left[D_1 - \gamma_{o4}\xi_{o4} - \frac{K_{i3}}{K_{i4}}(\beta_3 - \gamma_{o3}\xi_{o3})\right]e^{D_2(\frac{w_f}{2}-x_1)}} \\ & - \frac{\left\{-\frac{\xi_{o4}}{s} - \gamma_{o4}\xi_{o4}\frac{g_4(s)}{f_4(s)} + \frac{K_{i3}}{K_{i4}}\left[\beta_3\frac{g_3(s)}{f_3(s)} + \frac{\xi_{o3}}{s} - (\beta_3 - \gamma_{o3}\xi_{o3})\frac{g_4(s)}{f_4(s)}\right]\right\}\left(e^{D_1(x-\frac{w_f}{2})} - e^{D_2(x-\frac{w_f}{2})}\right)}{\left[D_2 - \gamma_{o4}\xi_{o4} - \frac{K_{i3}}{K_{i4}}(\beta_3 - \gamma_{o3}\xi_{o3})\right]e^{D_2(x_1-\frac{w_f}{2})} - \left[D_1 - \gamma_{o4}\xi_{o4} - \frac{K_{i3}}{K_{i4}}(\beta_3 - \gamma_{o3}\xi_{o3})\right]e^{D_1(x_1-\frac{w_f}{2})}} - \frac{g_4(s)}{f_4(s)}, \end{aligned} \tag{A27}$$

where

$$D_1 = \frac{G_{o4} + \sqrt{G_{o4}^2 + 4f_4(s)}}{2}, \tag{A28}$$

$$D_2 = \frac{G_{o4} - \sqrt{G_{o4}^2 + 4f_4(s)}}{2}, \tag{A29}$$

$$\xi_{o3} = \left(\frac{K_{ro}}{\mu_o B_o} + R_v\frac{K_{rg}}{\mu_g B_g}\right)\lambda_3, \tag{A30}$$

$$\xi_{o4} = \left(\frac{K_{ro}}{\mu_o B_o} + R_v \frac{K_{rg}}{\mu_g B_g}\right)\lambda_4. \tag{A31}$$

Appendix A.5. Region 5

By substituting Equations (27) and (28) into Equations (22)–(25), we obtain the zeroth-order equations for Region 5 as follows:

$$\begin{cases} \frac{\partial^2 \tau_{o05}}{\partial y^2} - G_{o5}\frac{\partial \tau_{o05}}{\partial y} + \frac{2}{w_f}\frac{K_{i4}}{K_{i5}}\left[\frac{\partial \tau_{o04}}{\partial x} + (1-\gamma_{o4}\tau_{o04})\left(\frac{K_{ro}}{\mu_o B_o} + R_v\frac{K_{rg}}{\mu_g B_g}\right)\lambda_4\right]\Big|_{x=\frac{w_f}{2}} = \frac{\phi_5 \eta_{o5}}{CK_{i5}}\frac{\partial \tau_{o05}}{\partial t}, \\ \tau_{o05}|_{t=0} = 0, \\ \frac{\partial \tau_{o05}}{\partial y}\Big|_{y=y_1} = 0, \\ \tau_{o05}|_{y=0} = \tau_{owf}, \end{cases} \tag{A32}$$

where $\tau_{owf} = \left[1 - e^{-\gamma_{o5}(p_{poi} - p_{powf})}\right]/\gamma_{o5}$.

Applying the Laplace transform to Equation (A32) with respect to t yields

$$\begin{cases} \frac{\partial^2 \overline{\tau}_{o05}}{\partial y^2} - G_{o5}\frac{\partial \overline{\tau}_{o05}}{\partial y} + \frac{2}{w_f}\frac{K_{i4}}{K_{i5}}\left[\frac{\partial \overline{\tau}_{o04}}{\partial x} + \left(\frac{1}{s} - \gamma_{o4}\overline{\tau}_{o04}\right)\left(\frac{K_{ro}}{\mu_o B_o} + R_v\frac{K_{rg}}{\mu_g B_g}\right)\lambda_4\right]\Big|_{x=\frac{w_f}{2}} = \frac{\phi_5 \eta_{o5}}{CK_{i5}} s\overline{\tau}_{o05}, \\ \frac{\partial \overline{\tau}_{o05}}{\partial y}\Big|_{y=y_1} = 0, \\ \overline{\tau}_{o05}|_{y=0} = \frac{\tau_{owf}}{s}. \end{cases} \tag{A33}$$

Based on Equation (A27), Equation (A33) can be rewritten as follows:

$$\begin{cases} \frac{\partial^2 \overline{\tau}_{o05}}{\partial y^2} - G_{o5}\frac{\partial \overline{\tau}_{o05}}{\partial y} - f_5(s)\overline{\tau}_{o05} = g_5(s), \\ \frac{\partial \overline{\tau}_{o05}}{\partial y}\Big|_{y=y_1} = 0, \\ \overline{\tau}_{o05}|_{y=0} = \frac{\tau_{owf}}{s}, \end{cases} \tag{A34}$$

where

$$f_5(s) = \frac{\phi_5 \eta_{o5} s}{CK_{i5}} - \frac{2}{w_f}\frac{K_{i4}}{K_{i5}}(\beta_4 - \gamma_{o4}\xi_{o4}), \tag{A35}$$

$$g_5(s) = -\frac{2}{w_f}\frac{K_{i4}}{K_{i5}}\left[\beta_4\frac{g_4(s)}{f_4(s)} + \alpha_4 + \frac{\xi_{o4}}{s}\right], \tag{A36}$$

$$\beta_4 = \frac{\left[D_2 - \gamma_{o4}\xi_{o4} - \frac{K_{i3}}{K_{i4}}(\beta_3 - \gamma_{o3}\xi_{o3})\right]D_1 e^{D_1(\frac{w_f}{2} - x_1)} - \left[D_1 - \gamma_{o4}\xi_{o4} - \frac{K_{i3}}{K_{i4}}(\beta_3 - \gamma_{o3}\xi_{o3})\right]D_2 e^{D_2(\frac{w_f}{2} - x_1)}}{\left[D_2 - \gamma_{o4}\xi_{o4} - \frac{K_{i3}}{K_{i4}}(\beta_3 - \gamma_{o3}\xi_{o3})\right]e^{D_1(\frac{w_f}{2} - x_1)} - \left[D_1 - \gamma_{o4}\xi_{o4} - \frac{K_{i3}}{K_{i4}}(\beta_3 - \gamma_{o3}\xi_{o3})\right]e^{D_2(\frac{w_f}{2} - x_1)}}, \tag{A37}$$

$$\alpha_4 = -\frac{\left\{-\frac{\xi_{o4}}{s} - \gamma_{o4}\xi_{o4}\frac{g_4(s)}{f_4(s)} + \frac{K_{i3}}{K_{i4}}\left[\beta_3\frac{g_3(s)}{f_3(s)} + \frac{\xi_{o3}}{s} - (\beta_3 - \gamma_{o3}\xi_{o3})\frac{g_4(s)}{f_4(s)}\right]\right\}(D_1 - D_2)}{\left[D_2 - \gamma_{o4}\xi_{o4} - \frac{K_{i3}}{K_{i4}}(\beta_3 - \gamma_{o3}\xi_{o3})\right]e^{D_2(x_1 - \frac{w_f}{2})} - \left[D_1 - \gamma_{o4}\xi_{o4} - \frac{K_{i3}}{K_{i4}}(\beta_3 - \gamma_{o3}\xi_{o3})\right]e^{D_1(x_1 - \frac{w_f}{2})}}, \tag{A38}$$

By solving Equation (A34), we derive the following analytical solution:

$$\overline{\tau}_{o05} = \frac{\left[\frac{\tau_{owf}}{s} + \frac{g_5(s)}{f_5(s)}\right]\left[E_2 e^{E_1(y-y_1)} - E_1 e^{E_2(y-y_1)}\right]}{E_2 e^{-E_1 y_1} - E_1 e^{-E_2 y_1}} - \frac{g_5(s)}{f_5(s)}, \tag{A39}$$

where

$$E_1 = \frac{G_{o5} + \sqrt{G_{o5}^2 + 4f_5(s)}}{2}, \tag{A40}$$

$$E_2 = \frac{G_{o5} - \sqrt{G_{o5}^2 + 4f_5(s)}}{2}. \tag{A41}$$

By applying the Pedrosa transformation and Laplace transform to Equation (26) and integrating the result with Equation (A39), we obtain

$$\bar{q}_o = -2Cn_f w_f h K_{i5}\left[(\beta_5 - \gamma_{o5}\xi_{o5})\frac{\tau_{owf}}{s} + \beta_5\frac{g_5(s)}{f_5(s)} + \frac{\xi_{o5}}{s}\right], \tag{A42}$$

where

$$\beta_5 = \frac{E_1E_2e^{-E_1y_1} - E_1E_2e^{-E_2y_1}}{E_2e^{-E_1y_1} - E_1e^{-E_2y_1}}, \tag{A43}$$

$$\xi_{o5} = \left(\frac{K_{ro}}{\mu_o B_o} + R_v\frac{K_{rg}}{\mu_g B_g}\right)\lambda_5. \tag{A44}$$

References

1. Lei, Q.; Xiong, W.; Yuan, J.; Gao, S.S.; Wu, Y.-S. Behavior of flow through low-permeability reservoirs. In Proceedings of the Europec/EAGE Conference and Exhibition, Rome, Italy, 9–12 June 2008.
2. Jiang, Z.; Zhang, W.; Liang, C.; Wang, Y.; Liu, H.; Chen, X. Basic characteristics and evaluation of shale oil reservoirs. *Pet. Res.* **2016**, *1*, 149–163. [CrossRef]
3. Liu, C. Numerical simulation of ultra-low permeability reservoirs: Progress and challenges. *Front. Energy Res.* **2022**, *10*, 895135. [CrossRef]
4. Hao, M.; Liu, X.; Xia, J.; Liu, Y. Study of nonlinear flow mechanisms and microfracture networks in low-permeability reservoirs. *Front. Earth Sci.* **2023**, *10*, 1015199. [CrossRef]
5. Li, Z.; Lei, Z.; Shen, W.; Martyushev, D.A.; Hu, X. A comprehensive review of the oil flow mechanism and numerical simulations in shale oil reservoirs. *Energies* **2023**, *16*, 3516. [CrossRef]
6. Yao, L.; Yang, Z.; Li, H.; Du, M.; Zhou, T.; Zhang, Y. Research on mathematical model of shale oil reservoir flow. *Energies* **2023**, *16*, 5452. [CrossRef]
7. Feng, Q.; Xu, S.; Xing, X.; Zhang, W.; Wang, S. Advances and challenges in shale oil development: A critical review. *Adv. Geo-Energy Res.* **2020**, *4*, 406–418. [CrossRef]
8. Li, R.; Chen, Z.; Wu, K.; Hao, X.; Xu, J. An analytical model for water-oil two-phase flow in inorganic nanopores in shale oil reservoirs. *Pet. Sci.* **2021**, *18*, 1776–1787. [CrossRef]
9. Yadav, D.; Kim, M.C. The onset of transient Soret-driven buoyancy convection in nanoparticle suspensions with particle-concentration-dependent viscosity in a porous medium. *J. Porous Media* **2015**, *18*, 369–378. [CrossRef]
10. Zhu, W.; Pan, B.; Chen, Z.; Bu, W.; Ma, Q.; Liu, K.; Yue, M. Transport in nanoporous media. *Engineering* **2024**, *32*, 138–151. [CrossRef]
11. Ren, J.; Lei, H. Lattice Boltzmann model for incompressible flows through porous media with time-fractional effects. *Commun. Nonlinear Sci. Numer. Simul.* **2024**, *135*, 108035. [CrossRef]
12. Clarkson, C.R. Production data analysis of unconventional gas wells: Review of theory and best practices. *Int. J. Coal Geol.* **2013**, *109*, 101–146. [CrossRef]
13. Zhou, W.; Banerjee, R.; Poe, B.D.; Spath, J.; Thambynayagam, M. Semianalytical production simulation of complex hydraulic-fracture networks. *SPE J.* **2014**, *19*, 6–18. [CrossRef]
14. Li, Q.; Xing, H.; Liu, J.; Liu, X. A review on hydraulic fracturing of unconventional reservoir. *Petroleum* **2015**, *1*, 8–15. [CrossRef]
15. Adekola, U.A.; Gimba, A.S.B.; Ayuba, S.; Jakada, K.; Okafor, I.S.; Nzerem, P.; Chior, T.; Ogolo, O.; Ibrahim, K.S. A comprehensive review of hydraulic fracturing techniques in shale gas production. *Nile J. Eng. Appl. Sci.* **2023**, *1*, 216–228. [CrossRef]
16. Zhao, M. Field experiments and main understanding of shale oil hydraulic fracturing. *Front. Earth Sci.* **2024**, *12*, 1410524. [CrossRef]
17. Lei, Q.; Xu, Y.; Cai, B.; Guan, B.; Wang, X.; Bi, G.; Li, H.; Li, S.; Ding, B.; Fu, H.; et al. Progress and prospects of horizontal well fracturing technology for shale oil and gas reservoirs. *Pet. Explor. Dev.* **2022**, *49*, 191–199. [CrossRef]
18. Liang, H.-B.; Zhang, L.-H.; Zhao, Y.-L.; Zhang, B.-N.; Chang, C.; Chen, M.; Bai, M.-X. Empirical methods of decline-curve analysis for shale gas reservoirs: Review, evaluation, and application. *J. Nat. Gas Sci. Eng.* **2020**, *83*, 103531. [CrossRef]
19. Tan, L.; Zuo, L.; Wang, B. Methods of decline curve analysis for shale gas reservoirs. *Energies* **2018**, *11*, 552. [CrossRef]
20. Boogar, A.S.; Gerami, S.; Masihi, M. Investigation into the capability of a modern decline curve analysis for gas condensate reservoirs. *Sci. Iran.* **2011**, *18*, 491–501.
21. Zhang, H.; Rietz, D.; Cagle, A.; Cocco, M.; Lee, J. Extended exponential decline curve analysis. *J. Nat. Gas Sci. Eng.* **2016**, *36*, 402–413. [CrossRef]
22. Manda, P.; Nkazi, D.B. The evaluation and sensitivity of decline curve modelling. *Energies* **2020**, *13*, 2765. [CrossRef]

23. Lee, S.T.; Brockenbrough, J.R. A new approximate analytic solution for finite-conductivity vertical fractures. *SPE Form. Eval.* **1986**, *1*, 75–88. [CrossRef]
24. Brown, M.; Ozkan, E.; Raghavan, R.; Kazemi, H. Practical solutions for pressure-transient responses of fractured horizontal wells in unconventional shale reservoirs. *SPE Reserv. Eval. Eng.* **2011**, *14*, 663–676. [CrossRef]
25. Stalgorova, E.; Mattar, L. Analytical model for unconventional multifractured composite systems. *SPE Reserv. Eval. Eng.* **2013**, *16*, 246–256. [CrossRef]
26. Wu, Z.; Cui, C.; Lv, G.; Bing, S.; Cao, G. A multi-linear transient pressure model for multistage fractured horizontal well in tight oil reservoirs with considering threshold pressure gradient and stress sensitivity. *J. Pet. Sci. Eng.* **2019**, *172*, 839–854. [CrossRef]
27. Bruce, G.H.; Peaceman, D.W.; Rachford, H.H., Jr.; Rice, G.D. Calculations of unsteady-state gas flow through porous media. *J. Pet. Technol.* **1953**, *5*, 79–92.
28. Yin, D.; Zhou, Y.; Yuan, H.; Zhang, C. The numerical simulation of non-Darcy flow for YuShulin low permeability oilfield. *Int. J. Control. Autom.* **2013**, *6*, 323–344.
29. Khamidullin, M.; Mazo, A.; Potashev, K. Numerical simulation of a one-phase steady flow towards a multistage fractured horizontal well. *Lobachevskii J. Math.* **2017**, *38*, 818–826. [CrossRef]
30. Luo, S.; Zhao, Y.; Zhang, L.; Chen, Z.; Zhang, X. Integrated simulation for hydraulic fracturing, productivity prediction, and optimization in tight conglomerate reservoirs. *Energy Fuels* **2021**, *35*, 14658–14670. [CrossRef]
31. Xiao, H.; Geng, S.; Luo, H.; Song, L.; Wang, H.; He, X. Numerical simulation of fractured horizontal well considering threshold pressure gradient, non-Darcy flow, and stress sensitivity. *Energy Sci. Eng.* **2023**, *11*, 811–825. [CrossRef]
32. Arps, J.J. Analysis of decline curves. *Trans. AIME* **1945**, *160*, 228–247. [CrossRef]
33. Valkó, P.P. Assigning value to stimulation in the Barnett Shale: A simultaneous analysis of 7000 plus production hystories and well completion records. In Proceedings of the SPE Hydraulic Fracturing Technology Conference, The Woodlands, TX, USA, 19–21 January 2009.
34. Duong, A.N. Rate-decline analysis for fracture-dominated shale reservoirs. *SPE Reserv. Eval. Eng.* **2011**, *14*, 377–387.
35. Deng, Q.; Nie, R.S.; Jia, Y.L.; Huang, X.Y.; Li, J.M.; Li, H.K. A new analytical model for non-uniformly distributed multi-fractured system in shale gas reservoirs. *J. Nat. Gas Sci. Eng.* **2015**, *27*, 719–737. [CrossRef]
36. Zhang, L.; Gao, J.; Hu, S.; Guo, J.; Liu, Q. Five-region flow model for MFHWs in dual porous shale gas reservoirs. *J. Nat. Gas Sci. Eng.* **2016**, *33*, 1316–1323. [CrossRef]
37. Haeri, F.; Izadi, M.; Zeidouni, M. Unconventional multi-fractured analytical solution using dual porosity model. *J. Nat. Gas Sci. Eng.* **2017**, *45*, 230–242. [CrossRef]
38. Ji, J.H.; Yao, Y.; Huang, S.; Ma, X.; Zhang, S.; Zhang, F. Analytical model for production performance analysis of multi-fractured horizontal well in tight oil reservoirs. *J. Pet. Sci. Eng.* **2017**, *158*, 380–397. [CrossRef]
39. Shi, D.; Lu, Z. Semianalytical model for flow behavior analysis of unconventional reservoirs with complex fracture distribution. *Geofluids* **2020**, *2020*, 9394140. [CrossRef]
40. Yuan, B.; Su, Y.; Moghanloo, R.G.; Rui, Z.; Wang, W.; Shang, Y. A new analytical multi-linear solution for gas flow toward fractured horizontal wells with different fracture intensity. *J. Nat. Gas Sci. Eng.* **2015**, *23*, 227–238. [CrossRef]
41. Zeng, J.; Wang, X.; Guo, J.; Zeng, F. Composite linear flow model for multi-fractured horizontal wells in heterogeneous shale reservoir. *J. Nat. Gas Sci. Eng.* **2017**, *38*, 527–548. [CrossRef]
42. Zeng, J.; Wang, X.; Guo, J.; Zeng, F.; Zhang, Q. Composite linear flow model for multi-fractured horizontal wells in tight sand reservoirs with the threshold pressure gradient. *J. Pet. Sci. Eng.* **2018**, *165*, 890–912. [CrossRef]
43. Guo, F.; Chen, R.; Yan, W.; Su, Y.; Hu, Y.; Xiong, S. A new seven-region flow model for deliverability evaluation of multiply-fractured horizontal well in tight oil fractal reservoir. *Fractals* **2023**, *31*, 2340173. [CrossRef]
44. Shojaei, H.; Tajer, E.S. Analytical solution of transient multiphase flow to a horizontal well with multiple hydraulic fractures. In Proceedings of the SPE Eastern Regional Meeting, Pittsburgh, PA, USA, 20–22 August 2013.
45. Zhang, M.; Becker, M.D.; Ayala, L.F. A similarity method approach for early-transient multiphase flow analysis of liquid-rich unconventional gas reservoirs. *J. Nat. Gas Sci. Eng.* **2016**, *28*, 572–586.
46. Behmanesh, H.; Mattar, L.; Thompson, J.M.; Anderson, D.M.; Nakaska, D.W.; Clarkson, C.R. Treatment of rate-transient analysis during boundary-dominated flow. *SPE J.* **2018**, *23*, 1145–1165. [CrossRef]
47. Wu, Y.; Cheng, L.; Huang, S.; Bai, Y.; Jia, P.; Wang, S.; Xu, B.; Chen, L. An approximate semianalytical method for two-phase flow analysis of liquid-rich shale gas and tight light-oil well. *J. Pet. Sci. Eng.* **2019**, *176*, 562–572. [CrossRef]
48. Luo, L.; Cheng, S.; Lee, J. Analytical model for rate transient analysis in low-permeability volatile oil reservoirs. In Proceedings of the SPE Annual Technical Conference and Exhibition, Calgary, AB, Canada, 30 September–2 October 2019.
49. Ke, W.; Luo, W.; Miao, S.; Chen, W.; Hou, Y. A transient productivity prediction model for horizontal wells coupled with oil and gas two-phase seepage and wellbore flow. *Processes* **2023**, *11*, 2012. [CrossRef]
50. Bai, W.; Cheng, S.; Wang, Y.; Cai, D.; Guo, X.; Guo, Q. A transient production prediction method for tight condensate gas well with multiphase flow. *Pet. Explor. Dev.* **2024**, *51*, 172–179. [CrossRef]

51. Zhang, Y.; Chen, Y.; Xu, A.; He, J.; Luo, E.; Liu, Y.; Zeng, X.; Jiang, L. Calculation method of three-phase productivity of horizontal well in water-bearing condensate gas reservoir. *Energies* **2024**, *17*, 2932.
52. Wei, B.; Qiao, R.; Hou, J.; Wu, Z.; Sun, J.; Zhang, Y.; Qiang, X.; Zhao, E. Multiphase production prediction of volume fracturing horizontal well in tight oil reservoir during cyclic water injection. *Phys. Fluids* **2025**, *37*, 013304. [CrossRef]
53. Pedrosa, O.A., Jr. Pressure transient response in stress-sensitive formations. In Proceedings of the SPE California Regional Meeting, Oakland, CA, USA, 2–4 April 1986.
54. Stehfest, H. Numerical inversion of Laplace transforms. *Commun. ACM* **1970**, *13*, 47–49. [CrossRef]
55. Ilk, D.; Blasingame, T.A. Decline curve analysis for unconventional reservoir systems-variable pressure drop case. In Proceedings of the SPE Unconventional Resources Conference Canada, Calgary, AB, Canada, 5–7 November 2013.

Disclaimer/Publisher's Note: The statements, opinions and data contained in all publications are solely those of the individual author(s) and contributor(s) and not of MDPI and/or the editor(s). MDPI and/or the editor(s) disclaim responsibility for any injury to people or property resulting from any ideas, methods, instructions or products referred to in the content.